

## Carbon

Yi Shi

### 1.1 Introduction

Carbon (C) is a nonmetallic element of period 2, group 14 (group IVA) of the periodic table, and the fourth most abundant element in the universe [1]. There are four valence electrons ( $2s^2 2p^2$ ) outside the carbon atom, meaning that all three types ( $sp$ ,  $sp^2$ ,  $sp^3$ ) of hybridization between  $s$ - and  $p$ -orbitals could occur in carbon atoms during the formation of chemical bonds. Due to the bonding characteristics, millions of organic compounds in which carbon atoms usually bond with other nonmetallic atoms (e.g. hydrogen, oxygen, nitrogen, etc.) or the C atom itself (forming carbon chain, branch, or ring structures) have been discovered in nature or synthesized artificially.

For elementary substances of carbon (not regarded as organic molecules but inorganic ones), different hybridization modes between carbon atoms lead to the diversity of structure and properties of its allotropes. Consider two typical types of carbon bulk materials: diamond is a three-dimensional (3D) network composed of  $sp^3$ -hybridized carbon, known as the hardest natural material, while graphite is a 3D structure stacked by a  $sp^2$ -hybridized carbon monolayer with a low degree of hardness but good lubricity. Carbon nanomaterials include diverse low-dimensional allotropes of carbon, such as graphene [2], graphene nanoribbons (GNRs) [3], carbon nanotubes (CNTs) [4], graphyne (GY) [5], fullerenes [6], and carbon dots (CDs) [7]. In contrast to natural bulk materials, theoretical research, practical preparation, and potential applications of carbon nanomaterials have only been in development for about one century. Nevertheless, numerous studies have demonstrated these carbon nanomaterials' unlimited promise with retained properties of bulk materials and unique properties of low-dimensional materials. In particular, the primary fabrication of two-dimensional (2D) graphene monolayers triggered an unprecedented graphene "gold rush" while opening the door to the two-dimensional materials (2DM) system, which is a historic step for the carbon nanomaterial system [8].

In this chapter, we will take graphene, CNTs, and GY as representative carbon nanomaterials and illustrate their fabrication methods, essential properties, and applications through recent frontier research findings.

## 1.2 Fabrication of Carbon Nanomaterials

### 1.2.1 Graphene

Graphene is a 2D building material for all other dimensions of  $sp^2$ -hybridized carbon materials, which can be transferred to zero-dimensional buckyballs (fullerenes), one-dimensional (1D) nanotubes, and 3D graphite (Figure 1.1) [8]. Although it was not until the early twenty-first century that graphene was isolated from bulk graphite, the concept of “graphene” or “monolayer graphite” had been proposed in the mid-twentieth century but initially used as a theoretical model that did not exist in a free state. This concept was derived from the conventional perspective proposed by Landau [9] and Peierls [10], who argued that 2D crystals could not exist independently because of their thermodynamic instability. For a long time afterward, atomic monolayer was considered to be obtained only by epitaxy on a 3D substrate. However, due to the interaction between the substrate and 2DM, epitaxial graphene may not entirely reflect the characteristics of “monolayer graphite.” Hence, researchers are still looking for methods to prepare independent graphene [11–13].

In fact, since the groundbreaking isolation of graphene monolayer [2], various top-down methods, such as micromechanical cleavage, liquid-phase exfoliation, and graphene oxide (GO) reduction, have successfully proved the independent existence of 2D crystals. Furthermore, aiming for the scalable application for the post-Moore era, bottom-up methods, such as confinement-controlled sublimation (CCS) and chemical vapor deposition (CVD), are actively used in large-scale, high-quality synthesis of graphene.

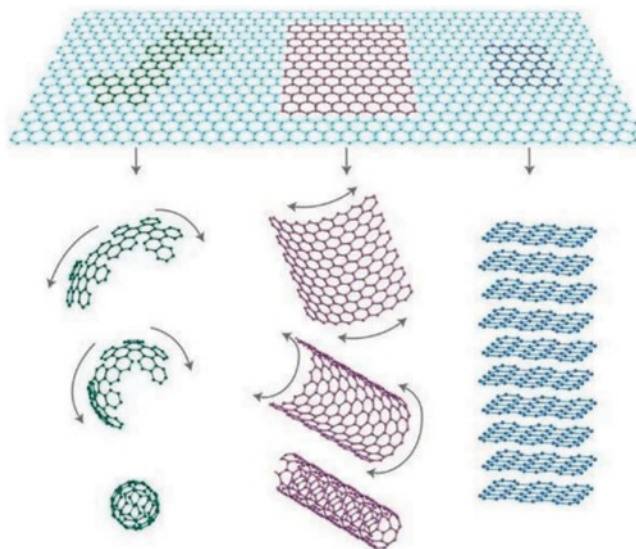


**Figure 1.1** The relationship between graphene and other carbon nanostructures. *Source:* Reprinted with permission from Ref. [8]. Copyright 2007, Springer Nature Limited.

### 1.2.1.1 Top-down Methods

#### 1.2.1.1.1 Dry Exfoliation of Graphene

In 2004, Novoselov et al. demonstrated the preparation of few-layer graphene (FLG) consisting of monolayer by micromechanical cleavage (repeated peeling by scotch tape) of highly oriented pyrolytic graphite [2]. This surprisingly simple method produced FLG films up to 10  $\mu\text{m}$  in size with stability and reliability (Figure 1.2a), and the properties of FLG are almost identical to those of theoretical studies. With convenience but low yield, the original cleavage method is suitable for research or proof of concept but not practical for large-scale applications. A layer-engineered exfoliation (LEE) technique was introduced by Moon et al. for large-area, layer-controlled graphene exfoliation (Figure 1.2b) [14]. In the LEE process, bulk natural graphite was firstly cleaved on adhesive tape, and then a selective metal film was directly deposited on the graphite by e-beam evaporation. The lattice mismatch between metal and graphite produced tensile stress at the interface, which created a crack at the boundaries of graphite induced by external bending and eventually led to large-area exfoliation of graphene [15]. The thickness of exfoliated graphene was determined by the difference between the metal-graphene binding energy ( $\gamma_{\text{metal-Gr}}$ ) and interlayer binding energy of graphite ( $\gamma_{\text{Gr-Gr}}$ ), resulting in a thicker layer with a higher difference (Figure 1.2b,c) [15, 16]. Due to the slight difference between  $\gamma_{\text{Au-Gr}}$  and  $\gamma_{\text{Gr-Gr}}$  Au-assisted LEE graphene showed a defect-free monolayer with a large lateral size of 1 mm and could be repeatedly exfoliated from the same bulk graphite (Figure 1.2d,e). The large-area exfoliation strategy controlled by interface binding energy between metal and 2DM is also applicable in other 2DM systems, such as transition metal dichalcogenides [17].

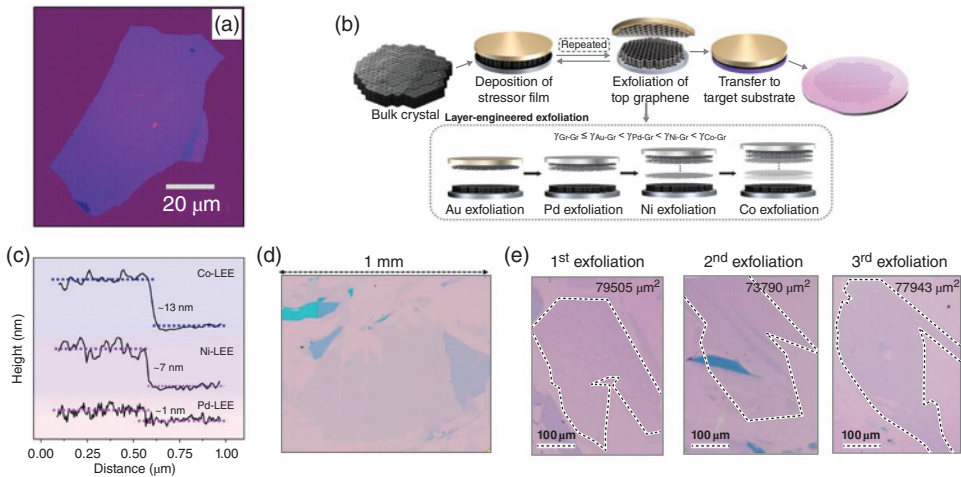


**Figure 1.2** (a) OM image of FLG produced using original micromechanical cleavage method. *Source:* Reprinted with permission from Ref. [2]. Copyright 2004, The American Association for the Advancement of Science. (b) Schematic of LEE process and the relation between  $\gamma_{\text{metal-Gr}}$  and  $\gamma_{\text{Gr-Gr}}$ . (c) AFM profile of Co-, Ni-, and Pd-LEE graphene with the relation  $\gamma_{\text{Pd-Gr}} < \gamma_{\text{Ni-Gr}} < \gamma_{\text{Co-Gr}}$ . (d) Low-magnification OM image of LEE graphene with millimeter-size monolayer. (e) OM images of repeated LEE graphene. *Source:* Reprinted with permission from Ref. [14]. Copyright 2020, The American Association for the Advancement of Science.

### 1.2.1.1.2 Liquid-phase Exfoliation of Graphene

Compared with air ambience, liquid immersion can significantly reduce the van der Waals (vdW) interaction between neighboring layers of graphite. With external forces induced by sonication [18], ball milling [19], or shear mixing [20], graphene nanosheets could be easily exfoliated in the liquid phase, generally provided by water or organic solvents. High tension at the solid/liquid interface hurts solid dispersion in a liquid medium. Therefore, the selection of a liquid medium can directly determine the quality of liquid-exfoliated graphene, and solvents with a lower surface tension ( $\gamma \sim 40 \text{ mN}\cdot\text{m}^{-2}$  [18]) could minimize the tension at the graphene/solvent interface [21]. Furthermore, adding surfactants or intercalation particles can also weaken the vdW interaction of graphite.

Supercritical fluid (SCF) is a special substance with a temperature and pressure above the critical point ( $T_c, p_c$ ), where liquid and gas phases cannot be distinct (Figure 1.3a). SCFs have specific intermediate properties between liquid and gas, such as gas-like diffusivity, liquid-like solubility, and adjustable density and viscosity controlled by temperature and pressure [22, 23]. Supercritical carbon dioxide (SCCO<sub>2</sub>), with an easily accessible critical point ( $T_c = 31.1^\circ\text{C}$ ,  $p_c = 7.38 \text{ MPa}$  [24]), is a suitable medium for graphene exfoliation owing to extremely low surface tension, shearing effect produced by complex hydrodynamics, and intercalation of CO<sub>2</sub> molecules. Zhu et al. characterized the SCCO<sub>2</sub>-exfoliated graphene and explained the stress mechanism in SCCO<sub>2</sub> applying on graphite (Figure 1.3b) [25].

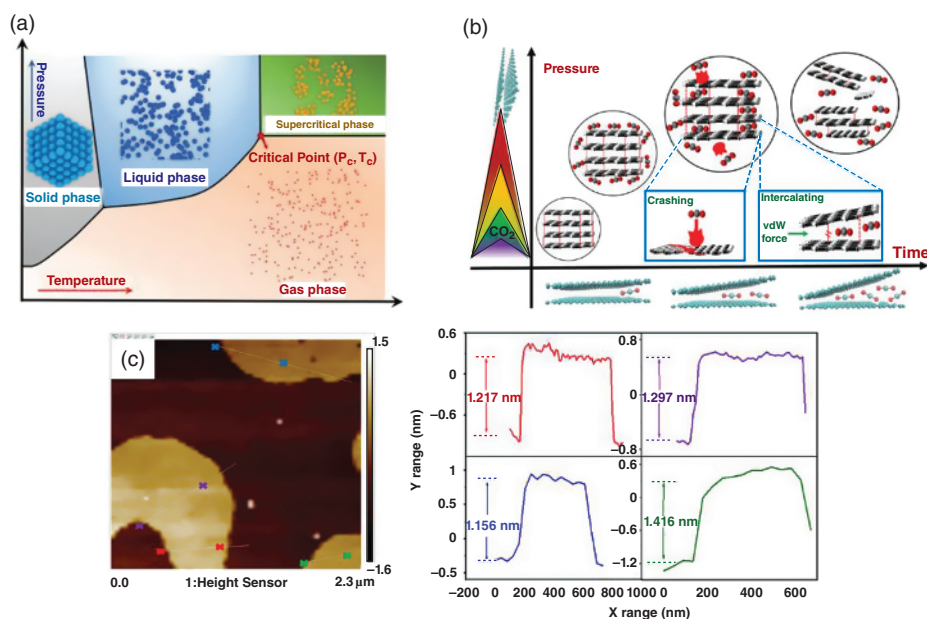


**Figure 1.3** (a) Schematic of a pressure–temperature phase diagram showing the supercritical region. *Source:* Reprinted with permission from Ref. [22]. Copyright 2023, Wiley-VCH GmbH. (b) Demonstration of SCCO<sub>2</sub>-assisted graphene exfoliation mechanism. (c) AFM image of graphene nanosheets with centrifugation posttreatment and corresponding height profiles along different labels. *Source:* Reprinted with permission from Ref. [25]. Copyright 2021, Elsevier Ltd.



Tangential stress could enhance the intercalation effect of  $\text{SCCO}_2$  on graphite's vdW gap, while the direct impact of normal stress on the graphene surface could break C—C bonds and reduce the size of graphene. The increasing pressure makes  $\text{SCCO}_2$  denser, enhancing the stress mechanism and leading to more efficient exfoliation. Longer processing time also contributes to complete exfoliation, but excessive processing will cause the agglomeration of graphene. Under the same posttreatment condition, graphene obtained at 45 MPa, 48 h showed the highest concentration with an average thickness of  $\sim 1.272$  nm, which could be regarded as two or three layers (Figure 1.3c).

### 1.2.1.1.3 Electrochemical Exfoliation

Electrochemical exfoliation (ECE) is still a liquid-phase intercalation method. However, the strong electric field generated by the ECE device allows the intercalation of larger ions or molecules, resulting in fast expansion and exfoliation of 2DM. A typical dual-electrode ECE device (Figure 1.4a) consists of a working electrode (usually

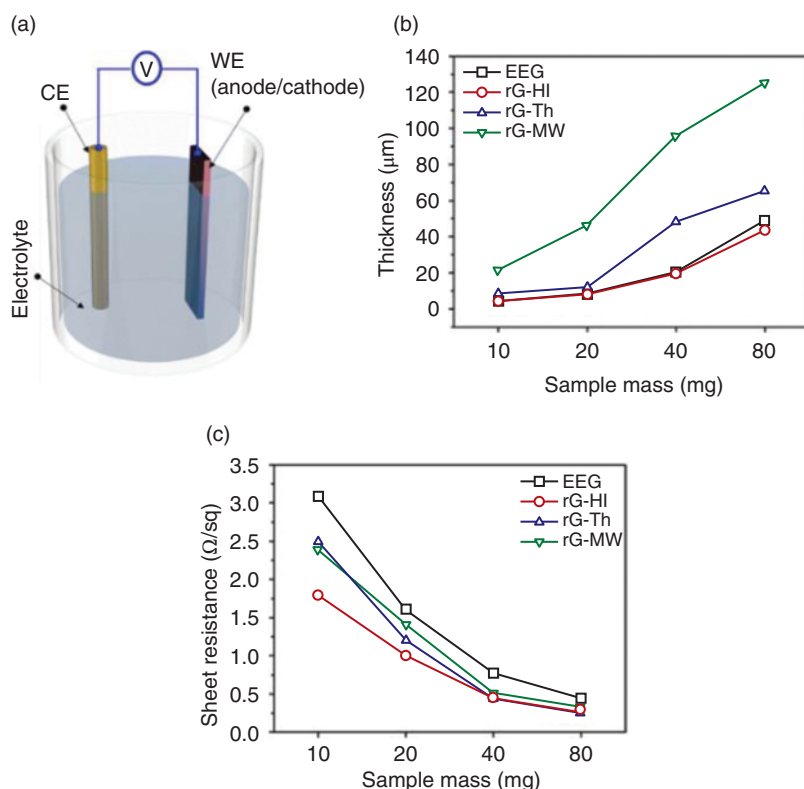


**Figure 1.4** (a) Schematic of a typical dual-electrode ECE setup. *Source:* Reprinted with permission from Ref. [26]. Copyright 2024, The Royal Society of Chemistry. (b) Thickness and (c) sheet resistance of electrochemically exfoliated graphene (EEG) and reduced graphene (rG) by HI, thermal (Th), and microwave (MW) treatment. *Source:* Reprinted with permission from Ref. [27]. Copyright 2021, American Chemical Society.

bulk materials for exfoliation such as graphite), a counter electrode (usually a metal plate), an electrolyte, and a power source [26]. According to charge characteristics of ions involved in intercalation, ECE can be classified into two types: anodic exfoliation, in which graphite acts as an anode to attract anions, and cathodic exfoliation, in which graphite acts as a cathode to attract cations. Anodic exfoliation is usually generated in an aqueous electrolyte containing anions such as  $\text{SO}_4^{2-}$ ,  $\text{ClO}_4^-$ ,  $\text{PO}_4^{3-}$ ,  $\text{OH}^-$ , and halide ( $\text{Cl}^-$ ,  $\text{Br}^-$ ,  $\text{I}^-$ ). Due to the positive voltage applied to graphite, anodic exfoliation provides higher productivity but inevitably leads to oxidation and defects in the exfoliated graphene [26, 27]. Mirkhani et al. proposed a high-temperature vapor reduction process to improve the morphology and electrical properties of graphene produced by anodic exfoliation [28]. Compared with thermal and microwave treatment, graphene with HI vapor treatment indicated a more compacted structure with more metallic luster and lower sheet resistance (Figure 1.4b,c). Cathodic exfoliation is a relatively mild process since the applied negative voltage could prevent graphene's oxidation, preserving its intrinsic properties. Nonaqueous media (e.g. *N*-methyl-2-pyrrolidone, dimethylformamide) containing cations such as alkali ions ( $\text{Li}^+$ ,  $\text{K}^+$ ,  $\text{Na}^+$ ) and quaternary ammonium ions (e.g. tetrapropylammonium, tetrabutylammonium) are commonly used for cathodic exfoliation of graphene. Most primary, secondary, and tertiary alkylammonium cations are unsuitable for cathodic exfoliation because of the instability under electrochemical potential. On the contrary, fully substituted quaternary ammonium ions can remain stable in this process [29]. However, limited by intercalation efficiency, the rate of the cathodic exfoliation process tends to be lower than that of the anodic exfoliation process [30, 31].

#### 1.2.1.1.4 Reduced Graphene Oxide

Reduced graphene oxide (rGO) is graphene obtained through the chemical oxidation of bulk graphite and subsequent reduction of GO. GO is typically synthesized by Brodie [32], Staudenmaier [33], or Hummers [34] method, which treats the graphite with a potent oxidizing agent (potassium chlorate or permanganate) in a robust acid environment (nitric acid or sulfuric acid) to promote interlayer spacing enlargement and conversion to GO. GO can be easily reduced to rGO by reaction with hydrazine or thermal annealing. However, using strong acids and oxidizing agents is undesirable for the mass production of rGO but also causes considerable structural defects and much residual oxygen in rGO [13, 35]. Tao et al. developed a novel catalyst-assisted exfoliation method for high-conductivity-dispersibility graphene (HCDG) with large lateral size (Figure 1.5a) [36]. The edge-oxidized graphite flake (eoGF) was produced through controllable oxidation, which differs from the conventional oxidation process. After the intercalation of the  $\text{Fe}^{3+}$  ion, eoGF was finally immersed in an  $\text{H}_2\text{O}_2$  solution and exfoliated into graphene sheets by the  $\text{Fe}^{3+}$ -catalyzed decomposition of  $\text{H}_2\text{O}_2$ . The generated  $\text{O}_2$  weakened the vdW interaction between eoGF layers without interior oxidization, which can be demonstrated in (002) characteristics of graphene determined using X-ray Diffraction (XRD), high-resolution transmission electron microscopy (Figure 1.5b,c), and localized, low-level oxidization determined using Raman spectra and X-ray Photoelectron Spectroscopy (XPS) (Figure 1.5d,e).

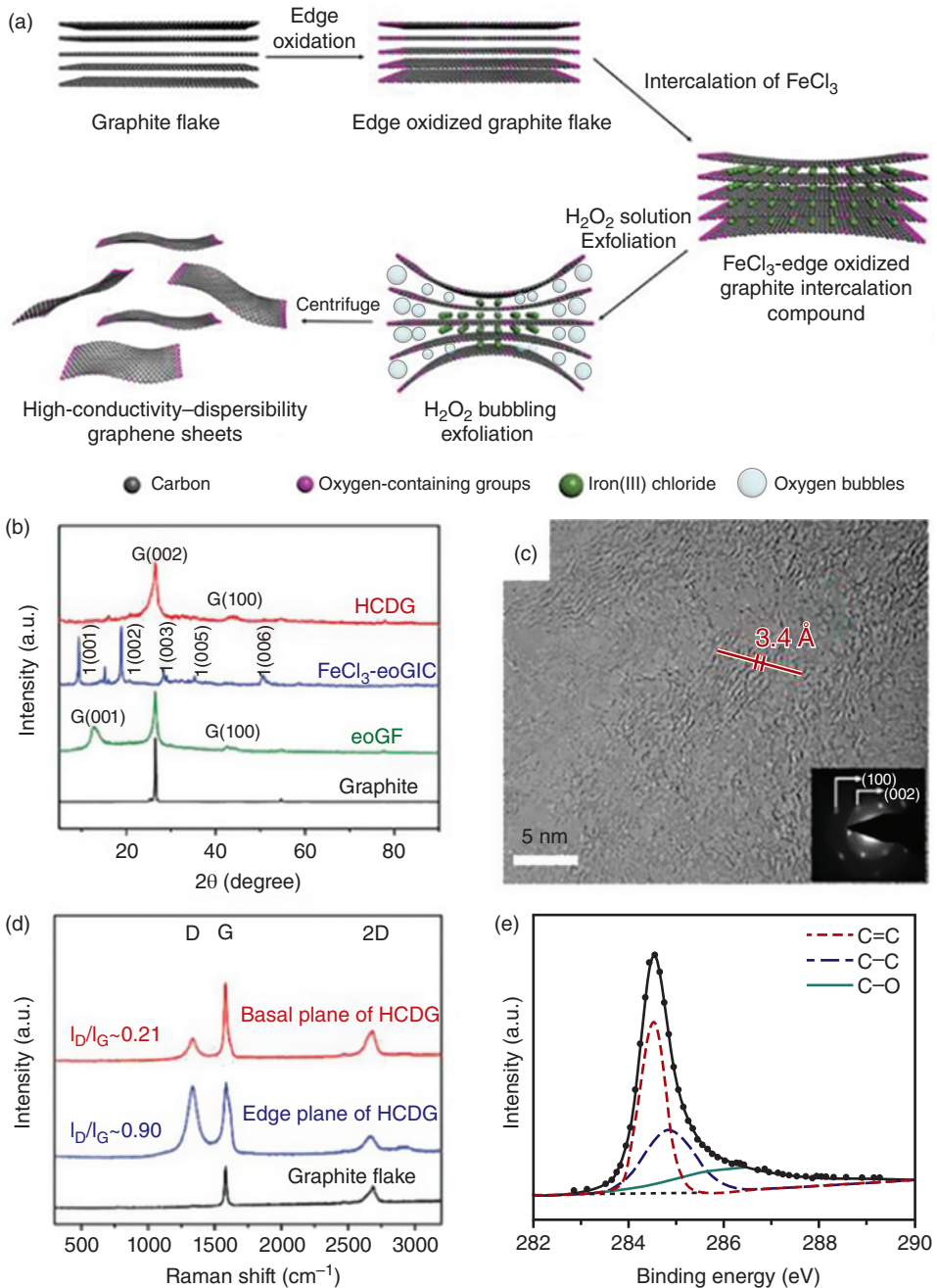


**Figure 1.5** (a) Schematics of catalyst-assisted exfoliation of HCDG. (b) XRD patterns of HCDG,  $\text{FeCl}_3$ -eoGIC, eoGF, and pristine graphite. (c) Transmission electron microscopy (TEM) image and selected area electron diffraction (SAED) pattern of the HCDG basal plane. (d) Raman spectra of HCDG and pristine graphite. (e)  $\text{C}1\text{s}$  spectra of XPS and deconvoluted peaks of HCDG. Source: Reprinted with permission from Ref. [36]. Copyright 2020, Wiley-VCH GmbH.

### 1.2.1.2 Bottom-up Methods

#### 1.2.1.2.1 Epitaxial Graphene on Silicon Carbide

As early as 1975, van Bommel et al. discovered the sublimation of silicon from SiC lattice and nucleation of a graphene layer in ultrahigh vacuum at  $\sim 800^\circ\text{C}$  [37]. Since the graphene layer was proved to be decoupled from SiC [38], graphene prepared using SiC high-temperature sublimation process was also called epitaxial graphene (epigraphene, EG). Zhao et al. demonstrated a quasi-equilibrium annealing method in which semiconductor epigraphene (SEG) is grown on macroscopic, atomically flat SiC terraces [39]. A CCS furnace with a small leak was designed for SEG growth (Figure 1.6a) [39, 40], in which graphene's growth rate depended on silicon atoms' escape rate. When the Si face of one SiC chip (acting as the seed) was placed oppositely to the C face of the other (acting as the source) in a CCS furnace at high temperature ( $>1600^\circ\text{C}$ ), due to the quasi-equilibrium between source and seed, subsequent step flow and step bunching occurred and eventually formed large SEG-coated (0001) facets on Si face (Figure 1.6b,c) [41]. This process differed from the depletion of the Si face in the conventional CCS process, with two Si faces placed oppositely. In addition, the SEG-covered (0001) facets were more stable than any other SiC facets, implying that wafer-level growth of single-crystal SEG should be possible in principle. Characterization of SEG showed a bandgap of 0.6 eV and ordered covalent bonds to SiC substrate, while there was no evidence of graphene on SiC ("SEG" and "graphene" cannot be equated). The electrical properties of SEG are described in Section 1.3.1.1.

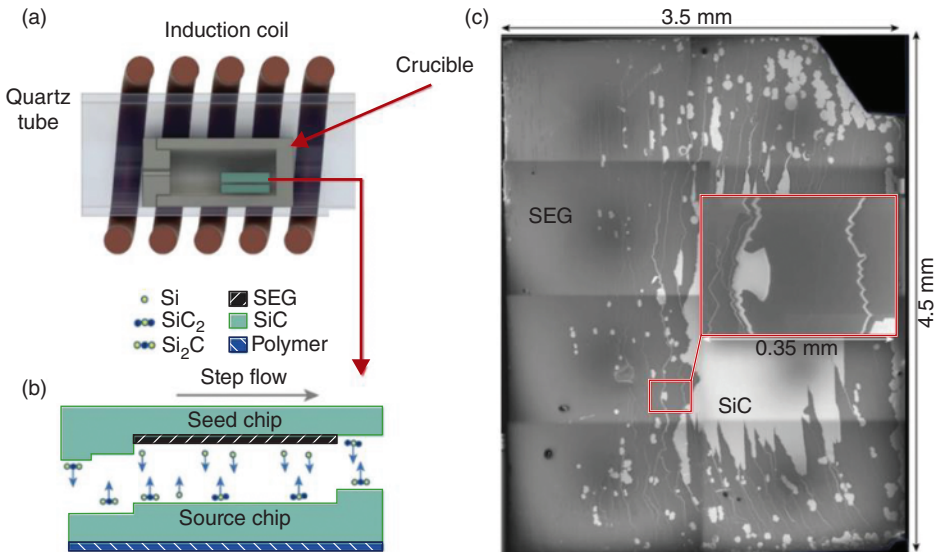


**Figure 1.6** (a) Schematic of a CCS furnace with two SiC chips inside a graphite crucible. (b) Schematic of two SiC chips stacked with the C face of the source chip facing the Si face of the seed chip. (c) Composite electron microscope image of a 3.5 mm  $\times$  4.5 mm SiC wafer with 80% SEG coverage. The localized area shows the contrast between SiC and SEG. *Source:* Reprinted with permission from Ref. [39]. Copyright 2024, Springer Nature Limited.

### 1.2.1.2.2 Chemical Vapor Deposition

CVD is a widely used process for the deposition of various kinds of material in microelectronics, such as metals, elemental or compound semiconductors, gate oxides, dielectrics, etc. In the graphene CVD process, gaseous precursors like hydrocarbons are primarily used for deposition, while solid [42, 43] and liquid [44] precursors are also feasible. Transition metal is a well-known substrate for graphene CVD, acting as a catalyst for dehydrogenating hydrocarbon precursors. Nucleation and growth of graphene ensue after the dehydrogenation process, and growth mechanisms on metal substrates can be divided into two categories according to the solubility of carbon in a specific metal. Ni and Cu are the two most commonly used metal substrates for graphene CVD, corresponding to the segregation growth mechanism on metals with higher carbon solubility and the surface growth mechanism on metals with lower carbon solubility. The segregation mechanism on Ni tends to grow into multilayer graphene, in which the thickness, crystalline state, and defect of Ni substrate will influence the morphology of graphene [45, 46]. The surface mechanism on Cu refers to a self-limiting and robust reaction process, which is more favorable for monolayer graphene growth [47]. However, due to the misorientation among different initial nuclei, the merging of crystal domains originating from these nuclei can only finally form polycrystalline graphene. Two strategies have been derived from this issue for the growth of large-scale, monocrystalline graphene on Cu: one is to reduce the nucleation density and maximize the expansion of a single nucleus, and the other is to achieve the perfect coalescence of domains by controlling the consistent orientation of multiple nuclei.

Through elaborate condition control and optimization, bilayer graphene (BLG) with AB (Bernal) stacking can be further produced on Cu. Zhang et al. achieved rapid CVD growth of large-area continuous BLG on Cu foil by introducing trace  $\text{CO}_2$  (Figure 1.7a) [48]. With the assistance of  $\text{CO}_2$ , ~50% BLG coverage could be achieved within 10 min based on the whole-covered monolayer graphene (MLG), and continuous BLG was obtained within 20 min. The growth mechanism of BLG was investigated by isotopic labeling with alternating introduction of  $^{13}\text{CH}_4$  and  $^{12}\text{CH}_4$ , which demonstrated that the second-layer graphene grew below the first layer and showed concentric rings composed of alternating  $^{12}\text{C}$  and  $^{13}\text{C}$  under Raman intensity mapping (Figure 1.7b–d). The introduced  $\text{CO}_2$  etched the first-layer graphene to form point defects, providing diffusion sites for the carbon source to form the second layer (Figure 1.7a), which differs from the conventional self-limiting growth mechanism on Cu. The AB-stacking structure was dominant in BLG, accounting for as high as 61% on Cu (100)-dominated polycrystalline Cu foils and 100% on super flat epitaxial single-crystal Cu (111) on annealed c-surface sapphire (Figure 1.7e,f). The  $\text{CO}_2$ -assisted strategy also showed high compatibility in submeter-scale ( $0.3 \text{ m} \times 0.1 \text{ m}$ ) substrates and roll-to-roll mass production, achieving more than 90% coverage of BLG.

## 1.2.2 Carbon Nanotubes

CNT is a type of seamless tubular graphite structure first prepared by Iijima in 1991 [4]. Although such 1D cylindrical tubular structure was rare in inorganic crystals at that time, Iijima predicted that structure engineering of carbon nanomaterials would be



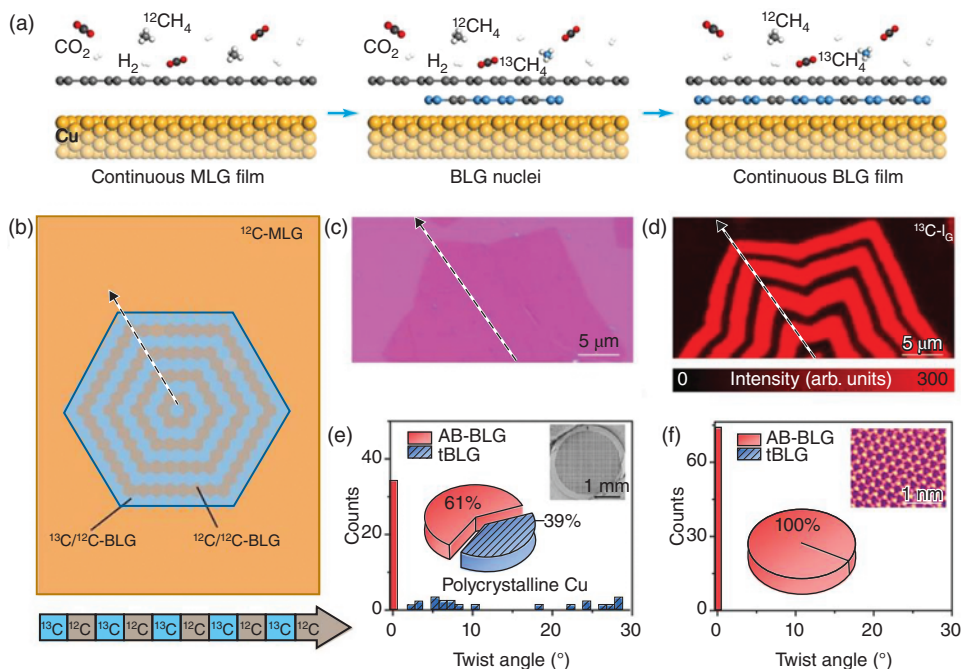


**Figure 1.7** (a) Schematic of CO<sub>2</sub>-assisted BLG growth through the alternating supplement of <sup>12</sup>CH<sub>4</sub> and <sup>13</sup>CH<sub>4</sub>. (b) Schematic of alternating <sup>12</sup>C and <sup>13</sup>C pattern of graphene. (c) OM image and (d) Raman intensity mapping of <sup>13</sup>C G-band of half BLG domain. (e, f) Distribution of twist angles based on SAED patterns of the BLG grown on (e) polycrystalline and (f) single-crystal Cu. *Source:* Reprinted with permission from Ref. [48]. Copyright 2023, Springer Nature Limited.

possible at much larger scales than fullerenes, which was confirmed by the first isolation of graphene in 2004 [2, 4]. According to the thickness of walls, CNTs can be classified into single-walled carbon nanotubes (SWCNTs) and multi-walled carbon nanotubes (MWCNTs). A SWCNT with a specific diameter can be regarded as the structure formed by the rotation and enclosure of a GNR monolayer around a particular vector, which can be described by a pair of chiral indices ( $n$ ,  $m$ ) (Figure 1.8) [49]. The relationship between  $n$  and  $m$  values reflects the configuration of SWCNTs [50, 51]. To be specific, SWCNTs with indices ( $n$ , 0) and ( $n$ ,  $n$ ) are called zigzag and armchair, which are two types with high symmetry. For  $n > m > 0$ , the indices ( $n$ ,  $m$ ) refer to a type of SWCNTs with chiral isomers. Chirality has an essential influence on the electrical properties of SWCNTs [52], which will be discussed in Section 1.3.2.

The main synthetic methods of CNTs are arc discharge (AD), laser ablation (LA), CVD, etc., which allow controlling and adjusting the morphology and parameters of CNTs by optimizing the growth conditions. In addition, since transition metal catalysts are necessary for the methods mentioned previously, the rational design of catalysts is also an effective strategy for controlled synthesis of CNTs [53].

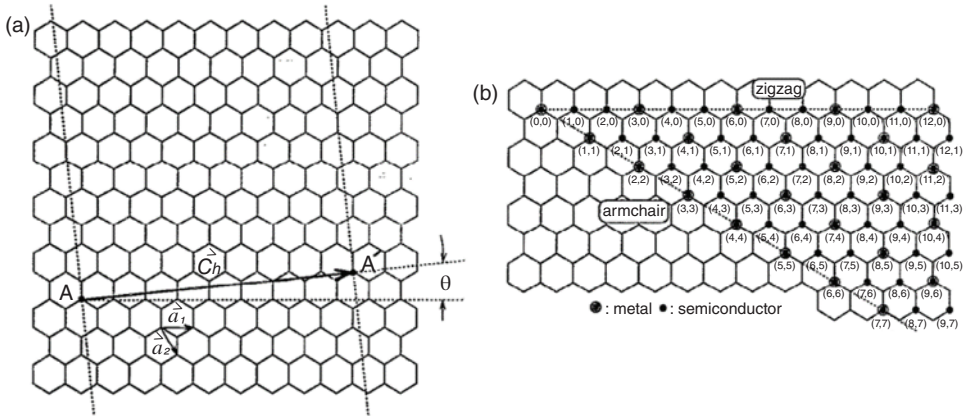


**Figure 1.8** (a) Chiral vector  $\vec{C}_h$  of a SWCNT in the unfolded 2D graphene layer. The unit vectors  $\vec{a}_1$  and  $\vec{a}_2$ , and chiral angle  $\theta$  are also shown. (b) Possible chiral indices with  $\theta$  ranging from  $0^\circ$  to  $30^\circ$ . The circled dots and dots denote each SWCNT's metallic and semiconducting behavior. *Source:* Reprinted with permission from Ref. [49]. Copyright 1992, American Institute of Physics.

### 1.2.2.1 Arc Discharge

The phenomenon of AD is usually generated by the approach of two electrodes under an inert ambiance. This principle was initially applied for the preparation of fullerenes, while CNTs were occasionally synthesized in this way by Iijima [4]. For AD synthesis of CNTs, graphite is used as both electrodes and high-temperature (above  $1500^\circ\text{C}$ ) plasma is generated by the arc under a large current, which causes the sublimation of carbon atoms from the anode and coagulation into CNTs on the cathode (Figure 1.9a) [54]. Therefore, the anode graphite is continuously consumed and designed to be mobile to maintain the

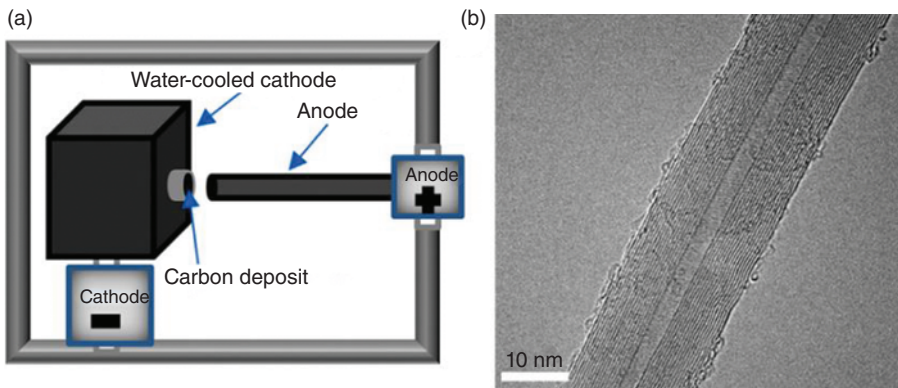


**Figure 1.9** (a) Schematic of CNT synthesis using AD. (b) High-resolution TEM image of MWCNTs synthesized using AD. *Source:* Reprinted with permission from Ref. [54]. Copyright 2022, Elsevier Ltd and Techna Group S.r.l.

optimum distance between two electrodes. However, AD-CNTs are often mixed with carbon-based by-products (e.g. amorphous carbon, fullerenes) and residual catalyst particles, which require further purification. Ribeiro et al. proposed a cyclic protocol of thermal oxidation and HCl solution reflux to purify AD-CNTs [55]. Each cycle was designed to oxidize and dissolve metal particles on the walls of CNTs and remove disordered or defect-rich carbon nanostructures, achieving an impurity removal efficiency of 66–75%. Moreover, due to the high ambient temperature, AD-CNTs always reveal an excellent crystallinity and straight morphology (Figure 1.9b) [54]; yet, elaborate control on parameters of CNTs, such as diameter, length, and chirality, is challenging to achieve by this method.

### 1.2.2.2 Laser Ablation

Similar to AD, the LA method for the synthesis of CNTs also involves the sublimation process of carbon atoms, which is dominated by a high-power laser under a high temperature ( $\sim 1200^\circ\text{C}$ ) (Figure 1.10a) [56]. Unlike the intermittent discharge process of AD, LA enables a continuous and efficient synthesis of CNTs with no requirement for the conductivity of carbon targets [56, 57]. Conventional LA process of CNTs used graphite target as a carbon source, while Chen et al. recently reported high-yield synthesis of SWCNT bundles using low-graphitized coal as a carbon source (Figure 1.10b) [57]. Despite complex carbon components and various impurity elements in coal, it is more easily ablated than graphite under the same LA conditions, resulting in a higher carbon evaporation rate. LA-SWCNTs synthesized from coal present an ideal distribution of diameter ( $\sim 1.1\text{--}1.3\text{ nm}$  at  $1198\text{ K}$ ) for electronic applications, which can be fabricated as the active layer of carbon nanotubes field effect transistors (CNT-FETs) (Figure 1.10c). However, it should be pointed out that the high-power laser in the LA setup prohibits its large-scale application to CNT synthesis [53].

### 1.2.2.3 Chemical Vapor Deposition

Due to the unacceptable condition of high temperatures in the AD and LA process, CVD is a suitable and mature alternative for synthesizing CNTs. On the one hand, according to the physical state of metal catalysts, typical substrate-supported catalyst CVD (SCCVD) mechanisms of CNTs can be classified into either vapor–solid–solid (VSS) or gas–liquid–solid

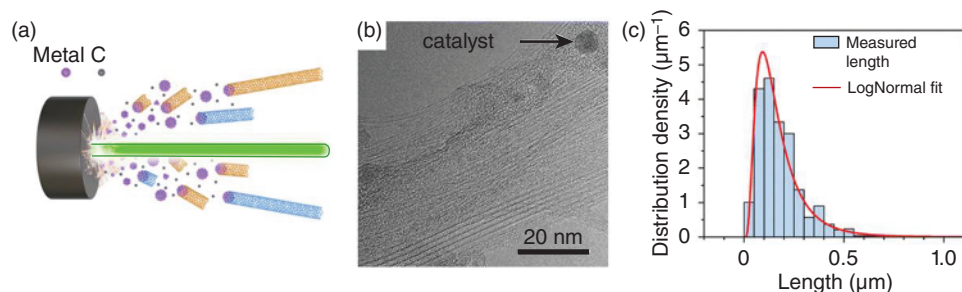


**Figure 1.10** (a) Schematic of CNT synthesis using LA. (b) TEM image of SWCNTs with marked catalyst. (c) Length distribution of SWCNTs sorted using PCz (poly[9-(1-octylonoyl)-9H-carbazole-2,7-diyl]). Source: Reprinted with permission from Ref. [57]. Copyright 2023, The Royal Society of Chemistry.

(VLS). In the VSS growth mechanism, the solid catalyst usually maintains a relatively stable morphology, and the precipitation of carbon atoms only happens on the catalyst's surface. The structure and components of the catalyst can be manipulated to narrow the diameter and chirality distribution of CNTs [58, 59]. In the VLS mechanism, the liquid state of the catalyst will lead to the dissolution of carbon and the movement of the catalyst droplet. Hence, the chirality of the synthesized CNT is randomly distributed.

On the other hand, as CVD growth progresses, the catalyst may eventually be located at the base or the tip of CNTs. VSS growth of CNTs may follow a base- or tip-growth mechanism, which is related to the strength of the interaction between catalyst metal and substrate, and the growth direction (vertical or parallel to substrates) of CNTs can be adjusted by plasma or airflow [60, 61]. VLS growth of CNTs is generally regarded as a tip-growth mechanism [62], as carbon atoms are only precipitated at the migrating catalyst droplet.

Different from metal catalyst pre-deposition in SCCVD methods, floating catalyst CVD (FCCVD) introduces catalyst precursor and gaseous carbon source together into the reaction chamber, followed by catalyst formation, carbon nucleation, and CNT growth [63, 64]. FCCVD-CNTs are usually floating in the chamber, which can be blown out with airflow and collected easily [65]. However, due to the short reaction time in the flowing atmosphere, CNTs are blown out without sufficient growth, exhibiting short lengths and random alignment. Jiang et al. proposed a substrate interception and orientation strategy (SIDS) to fabricate high-density ultralong CNT arrays by combining the so-called “kite-mechanism” (tip-growth mechanism) of ultralong CNTs with an improvement of FCCVD (Figure 1.11a,b) [66]. A substrate was placed horizontally into the center of the FCCVD chamber and used to intercept and reorient the floating short CNTs, which is absent in conventional FCCVD (Figure 1.11c,d). Local turbulence at the edge of the substrate caused one end of the CNTs to be anchored to the vertical step of the substrate, which sequentially followed the kite-like growth mechanism with an adequate flowing supply of carbon source (Figure 1.11e–g). Conventional growth of ultralong CNTs was based on VSS methods. In this case, the tip-growing CNTs initially need to overcome external forces such as vdW and drag forces to grow vertically without lying on the substrate [61, 67]. Actually, these dead CNTs account for a considerable portion of the total, resulting in a low catalyst utilization rate and CNT density [67].

### 1.2.3 Graphyne

GY is a type of 2D carbon nanostructure predicted by Baughman et al. in 1987, in which  $sp$ - and  $sp^2$ -hybridized carbon atoms coexist [68]. In GY structures, benzene rings are connected by acetylene bonds and form a hexagonal symmetric network, resulting in four types of chemical bonds with different lengths between carbon atoms: (i)  $C_{sp^2}-C_{sp^2}$  bonds in benzene rings; (ii)  $C_{sp} \equiv C_{sp}$  acetylene bonds; (iii)  $C_{sp^2}-C_{sp}$  bonds between benzene ring and acetylene bond; and (iv)  $C_{sp}-C_{sp}$  bonds between two acetylene bonds [69]. According to the number ( $n$ ) of acetylene bonds between two benzene rings, GY family can be typically classified into GY ( $n = 1$ ), graphdiyne (GDY) ( $n = 2$ ), graphtriyne ( $n = 3$ ), and graphtetrayne ( $n = 4$ ), or uniformly indicated by GY- $n$  (Figure 1.12) [70]. Among them, GDY is one of the most widely studied GY structures, which was first synthesized by Li et al. in 2010 [5].



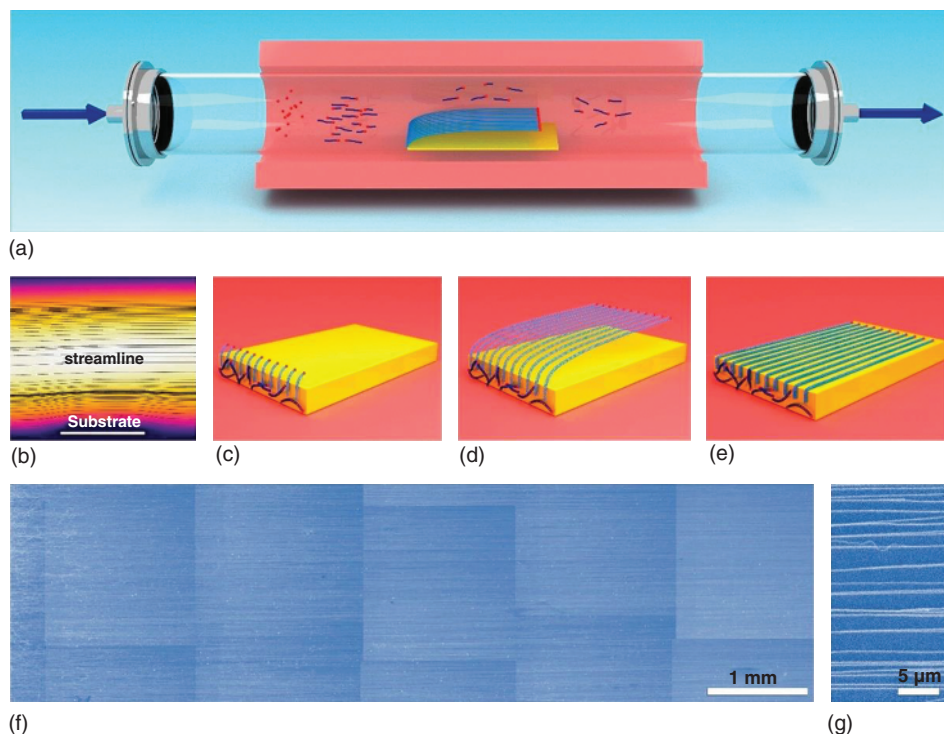


**Figure 1.11** (a) Schematic of ultralong CNT synthesis using SIDS. (b) CFD simulation of the velocity distribution and streamlines adjacent to the substrate. (c–e) Schematics of (c) interception, (d) reorientation and growth, and (e) the resultant array of ultralong CNTs during the FCCVD process with SIDS. (f, g) Scanning electron microscopy (SEM) image of the high-density ultralong CNT arrays with different scale bars. *Source:* Reprinted with permission from Ref. [66]. Copyright 2023, American Chemical Society.

GDY synthesis largely depends on the formation of diacetylene bonds, which can be achieved through an alkyne coupling reaction between two aryl monomers. In the early stages of exploring the synthesis of GDY, studies mainly focused on synthesizing several substructures of GDY or nanoGDY due to the difficulty in controlling the conditions for large ordered couplings [71]. The large-area synthesis of GDY was not extensively studied

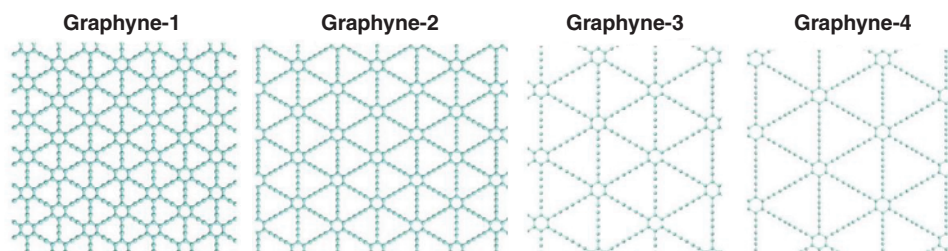


**Figure 1.12** GY containing different numbers ( $n = 1, 2, 3, 4$ ) of inserted acetylene bonds. *Source:* Reprinted with permission from Ref. [70]. Copyright 2023, American Chemical Society.



until Li et al. introduced the cross-coupling reaction of hexaethylbenzene (HEB) and demonstrated the obtained nanoscale GDY films [5]. According to the physical state of the substrate, GDY synthesis can be mainly classified into liquid-phase and solid-phase synthesis.

### 1.2.3.1 Liquid-phase Synthesis

The initial synthesis of GDY developed by Li et al. was carried out in a liquid-phase environment provided by tetrahydrofuran [5]. The cross-coupling reaction of HEB was driven by the release of trace Cu(II) ions from the Cu foil in an alkaline environment provided by pyridine, which ultimately formed a GDY thin film on Cu. Hence, the Cu foil served a dual role as catalyst and substrate [72]. Li et al. synthesized crystalline GDY (6L,  $\sim 2.19$  nm) through a modified Glaser–Hay coupling reaction of HEB and directly observed the rhombohedral (ABC) stacking in GDY by low-voltage TEM (Figure 1.13a,b) [73]. Direct characterization of few-layered GDY crystals is difficult due to structural fragility. Apart from growth at the liquid/solid interface, GDY can also grow at liquid/liquid and liquid/gas interfaces [74, 75]. Liquid/liquid interface is usually provided by water and water-immiscible organic solvents. During the reaction process, the catalyst in the aqueous phase and monomers in the organic phase undergo a coupling reaction at the interface and gradually grow into a suspended GDY layer, which can be easily transferred to other substrates using Langmuir–Schäfer method (Figure 1.13c,d). The stability of the liquid/liquid interface can effectively avoid the random interaction between monomer and catalyst [74]. The thickness of GDY can be adjusted by changing the concentrations of monomer and catalyst. GDY modification can be achieved by adding metal ions to the aqueous phase to form metal-GDY composite structures [76].

Besides interface-mediated synthesis, GDY can be synthesized directly in the liquid phase through coupling reaction. He et al. proposed a mild, convenient, and tunable one-pot method for the synthesis of GDY through Pd-catalyzed decarboxylation coupling reaction (Figure 1.14a) [77]. The synthesized GDY was characterized by typical 2D structure, high degree of crystallinity, and exhibited localized folding behaviors (Figure 1.14b,c). Li et al. proposed a space-confined synthesis method using MXene as a

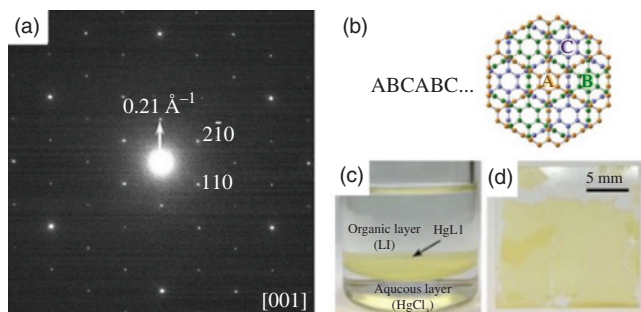


**Figure 1.13** (a) Experimental SAED pattern and (b) schematic stacking mode of ABC-stacked GDY. *Source:* Reprinted with permission from Ref. [73]. Copyright 2018, Tsinghua University Press and Springer-Verlag GmbH Germany. (c, d) Multilayer **Hg<sub>4</sub>L1** (L1=tris(4-ethynylphenyl)amine) nanosheets (c) at the liquid/liquid interface and (d) on a slide glass. *Source:* Reprinted with permission from Ref. [75]. Copyright 2021, Wiley-VCH GmbH.)

template for precise control of GDY's thickness and long-range ordering (Figure 1.14d) [78]. The sub-nanometer-sized gap between MXene layers allows monomers to be intercalated and coupled in situ and effectively constrains the out-of-plane growth or vertical stacking of GDY, ultimately yielding ML-GDY within MXene layers (Figure 1.14e). By liquid-phase exfoliation, 2DM mixtures containing free-standing ML-GDY with a lateral size distribution of 0.3–2.4  $\mu\text{m}$  could be obtained, in which the monolayer thickness and ordered in-plane structure of GDY were preserved (Figure 1.14f). Yan et al. directly exfoliated GDY bulk materials into monolayer or multilayer sheets by the assistance of  $\text{Li}_2\text{SiF}_6$  inorganic salt (Figure 1.14g) [79]. The most challenging aspect of GDY exfoliation is the potential introduction of structural defects or internal oxidation, which may affect the properties and application value of the eGDY. The noncovalent interactions generated by  $\text{SiF}_6^{2-}$  and the intercalation of small-radius  $\text{Li}^+$  together contributed to the efficient exfoliation and the preservation of GDY's original crystal structure without generating additional oxides (Figure 1.14h,i).

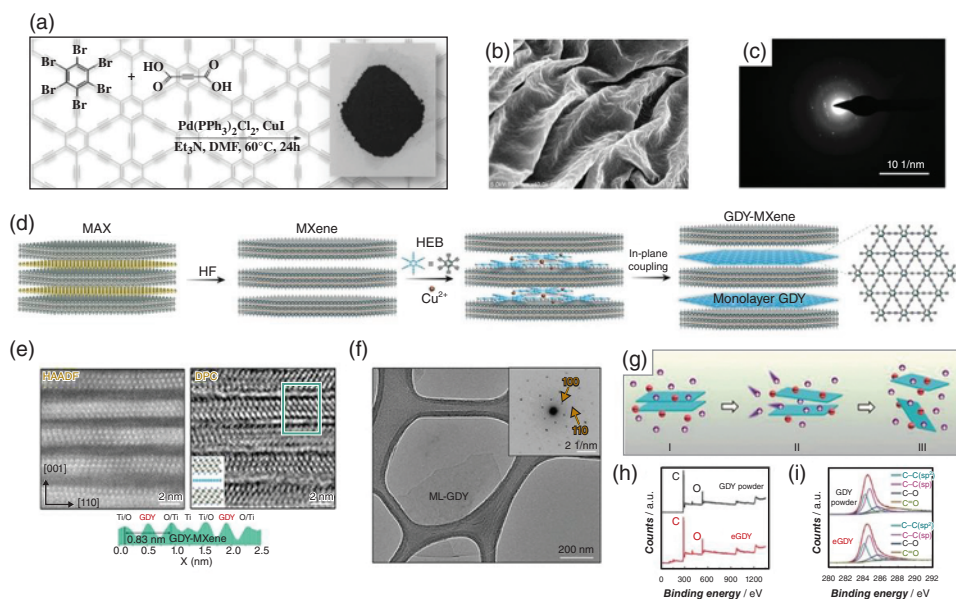


**Figure 1.14** (a) Schematic of GDY synthesis by decarboxylation coupling reaction. (b) The SEM image and (c) SAED pattern of GDY. *Source:* Reprinted with permission from Ref. [77]. Copyright 2023, The Royal Society of Chemistry. (d) Schematics of MXene template strategy for multilayer graphdiyne (MLGDY) synthesis. (e) High Angle Angular Dark Field-Scanning Transmission Electron Microscopy (HAADF-STEM) and Integrated Differential Phase Contrast Transmission Electron Microscopy (IDPC-STEM) of GDY-MXene structure along the [001] axis. The image intensity profile from the marked area is shown below. (f) TEM image and SAED pattern (inset) of free-standing monolayer GDY (ML-GDY). *Source:* Reprinted with permission from Ref. [78]. Copyright 2023, Wiley-VCH GmbH. (g) Salt-assisted exfoliation mechanism of GDY by three steps. Step I: adsorption of anions and cations on GDY; Step II: intercalation of cations into the charged interlayer; Step III: dispersed GDY in salt solution. (h) Wide-range XPS and (i) C1s spectra of bulk GDY powder and exfoliated GDY (eGDY). *Source:* Reprinted with permission from Ref. [79]. Copyright 2019, Wiley-VCH Verlag GmbH & Co. KGaA, Weinheim.

### 1.2.3.2 Solid-phase Synthesis

Metal-catalyzed, self-limited CVD is also suitable for GDY synthesis (Figure 1.15a,b). Although Cu maintains a high catalytic activity in the liquid-phase synthesis of GDY, in the case of CVD, Ag is more advisable than Cu as a catalyst and substrate for coupling. Unlike graphene CVD using gaseous carbon precursors such as  $\text{CH}_4$ , the CVD process of GDY must be kept at a low temperature to prevent the destruction of the aryl precursor [80]. Liu et al. obtained large ML-GDY films on Ag foils with hexaethynylbenzene (HEB) or 1,3,5-triethynylbenzene (TEB) as precursor at  $150^\circ\text{C}$ , which could be transferred by a standard PMMA process for further characterization (Figure 1.15c,d) [80]. Mechanical forces such as ball milling have also been proven to be an effective option for driving solvent-free, alkyne-based coupling reactions without catalyst assistance. Li et al. prepared pure GDY by ball-milling-driven reaction of calcium carbide ( $\text{CaC}_2$ ) and hexabromobenzene and confirmed the 1 : 1  $sp/sp^2$ -hybridized carbon ratio of GDY by characterization (Figure 1.15e,f) [81]. Previously, the group had successfully prepared hydrogen-substituted GDY by mechanochemical coupling of  $\text{CaC}_2$  and 1,3,5-tribromobenzene [82].

## 1.3 Properties and Applications of Carbon Nanomaterials

### 1.3.1 Graphene

According to the 1995 IUPAC Recommended Terminology, the term “graphene” was initially used to describe a single carbon layer with a graphitic structure, which should be used only when discussing the reactions, structural relations, or other properties of individual layers [83, 84]. In fact, with the increase in the number of stacked graphene monolayers, band

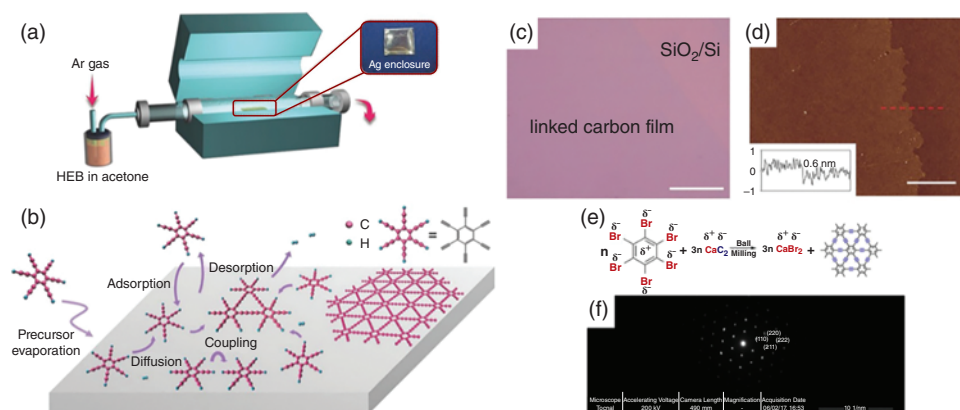


**Figure 1.15** (a, b) Schematics of (a) CVD system for GDY growth on Ag and (b) the surface growth process using HEB as a precursor. (c) Optical microscopy (OM) and (d) Atomic force microscopy (AFM) images of GDY film transferred on  $\text{SiO}_2/\text{Si}$  substrate. Inset in (d): height profile along the dashed line. Scale bars: (i) 50  $\mu\text{m}$  and (ii) 1  $\mu\text{m}$ . *Source:* Reprinted with permission from Ref. [80]. Copyright 2017, Wiley-VCH Verlag GmbH & Co. KGaA, Weinheim. (e) Ball-milling-driven reaction for GDY preparation. (f) SAED pattern of as-prepared GDY. *Source:* Reprinted with permission from Ref. [81]. Copyright 2018, Elsevier Ltd.

structure evolves rapidly and approaches the 3D limit of graphite at 10 layers [8, 85]. Thus, the meaning of “graphene” extends from monolayer to 2D stacked systems of up to 10 layers, and it is crucial to make a distinction when focusing on such materials. When discussing specific properties, especially electrical properties, it is necessary to classify graphene into MLG, BLG, trilayer (TLG), and multilayer (<10 layers), as the difference in properties due to the variation in the number of layers will lead to different applications for these graphene structures.

### 1.3.1.1 Electrical Properties and Applications

Under the tight-binding approximation, intrinsic MLG shows a linear dispersion relation in its Brillouin zone at the K and K' points (Dirac points) [86, 87]. MLG's conduction and valence bands intersect at Dirac points; hence, it behaves as a zero-bandgap semimetal. Due to the ballistic transport properties of carriers, graphene can exhibit high mobility (theoretical maximum of  $\sim 200\,000\text{ cm}^2/(\text{V}\cdot\text{s})$  at room temperature (RT) [88]), while the lack of bandgap becomes a major stumbling block for carrier modulation, which creates difficulties in the application of graphene field effect transistors (GFETs). Therefore, effective carrier modulation methods can significantly improve the performance of GFETs and highlight the advantage of high mobility. Zheng et al. introduced a graphene strain-effect transistor (GSET), which restricts and recovers current conduction through reversible nanocrack in the source/drain metal contacts (Figure 1.16a,b), resulting in a vast  $I_{\text{ON}}/I_{\text{OFF}}$  ratio of over  $10^7$  [89]. When a back-gate voltage exceeding the switching threshold ( $|V_{\text{BG}}| > |V_{\text{ST}}|$ ) was applied to GSET, the piezoelectric lead zirconate titanate back-gate dielectric strained on the Ni/Au contacts and eventually switched off the GSET. The contrary ambipolar characteristics (OFF–ON–OFF) of GSET were quite different from the conventional ambipolar characteristics (ON–OFF–ON) (Figure 1.16c). Furthermore, the switching threshold voltages ( $V_{\text{ST,P}}$  and  $V_{\text{ST,N}}$ ) of GSET tended to stabilize after a 17-strain cycling process (Figure 1.16d), suggesting a reversible strain mechanism. In the ON-state ( $|V_{\text{BG}}| < |V_{\text{ST,N}}|$  and  $|V_{\text{BG}}| < |V_{\text{ST,P}}|$ ), GSET exhibited linear output characteristics, indicating the semimetallic nature of graphene.

vdW heterostructure combines different 2DM through vdW interactions, offering preparation flexibility and good interfacial contacts [91]. Bai et al. achieved complementary properties between graphene and  $\text{WS}_2$  by preparing highly tunable field-effect tunneling transistors (FETTs) with vertically stacked graphene-hBN-graphene- $\text{WS}_2$ -graphene heterostructure (Figure 1.16h) [90]. Multilayer  $\text{WS}_2$  has a suitable indirect bandgap of 1.4 eV [92], which enables the alignment between the Fermi level of graphene and the conduction band minimum of  $\text{WS}_2$  and contributes to efficient carrier tunneling. In graphene- $\text{WS}_2$ -graphene (GWG) heterostructure, the barrier shape was modulated by the bias voltage ( $V_b$ ) between the bottom (B-Gr) and top graphene layer (T-Gr), which switched the tunneling mechanism between direct tunneling under a small  $V_b$  and Fowler–Nordheim tunneling under a large  $V_b$  (Figure 1.16i–k). GWG-FETTs also changed the operating states through  $V_b$  between n-type and bipolar complementary metal oxide semiconductor-like tunneling devices (Figure 1.16). Moreover, the thermionic emission mechanism was proved to contribute significantly to the on-current of FETTs (Figure 1.16l), as evidenced by high  $I_{\text{ON}}/I_{\text{OFF}}$  ratios of  $1.5 \times 10^6$  and  $5 \times 10^8$  at RT (300 K) and low temperature (5 K), respectively, under small  $V_b$ .

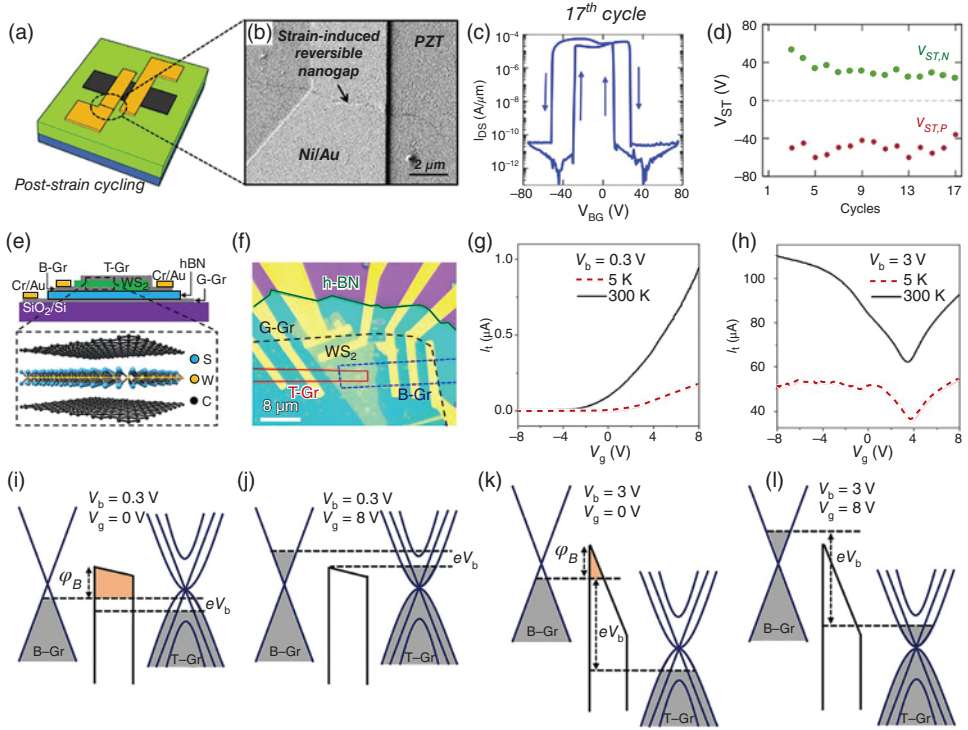


**Figure 1.16** (a) 3D schematic of the post-strain cycling process of GSET. (b) SEM image of the strain-induced nanogap across Ni/Au contact. (c) Transfer characteristics of GSET at the 17<sup>th</sup> strain cycle. (d) Switching threshold voltages ( $V_{ST,P}$  and  $V_{ST,N}$ ) of GSET in 17 strain cycles. *Source:* Reprinted with permission from Ref. [89]. Copyright 2023, American Chemical Society. (e) Schematics of GWG-FETT with the crystalline structure of each layer shown in the enlarged view. (f) OM image of GWG-FETT. (g, h) Corresponding transfer curves of GWG-FETT at (g)  $V_b = 0.3$  V and (h)  $V_b = 3$  V. (i-l) Energy band alignment diagrams at (i, j)  $V_b = 0.3$  V and (k, l)  $V_b = 3$  V under zero and positive  $V_g$ . *Source:* Reprinted with permission from Ref. [90]. Copyright 2022, American Chemical Society.

The switching performance of GFETs can also be improved by modifying the band structure of graphene. In the pioneering report by Novoselov et al., the degree of energy band overlap ( $\delta\epsilon$ ) varied in FLGs with different thicknesses, and the thinnest FLG sample was considered to possess a zero bandgap [2]. The  $\delta\epsilon$  overlap could be used to account for the inversion of Hall coefficients ( $R_H$ ) in FLG with the variation of gate voltage ( $V_G$ ) (Figure 1.17a), suggesting that FLG could be transformed from mixed-carrier material to either fully electronic or entirely hole conductor. Li et al. introduced a bandgap by changing the hybridization form of carbon atoms in graphene (Figure 1.17b) [93]. A reversible hydrogenation process realized this transition in a highly concentrated hydrogen-ion electrolyte, in which the electric field generated by  $V_G$  induced the hydrogen adsorption and desorption on GFETs. When the positive  $V_G$  increased above the hydrogenation potential, the graphene lattice became highly activated and transformed into  $sp^3$ -hybridized insulating hydrogenated graphene. As  $V_G$  was swept back to negative, the gradual increase in  $I_{DS}$  indicated the recovery of graphene



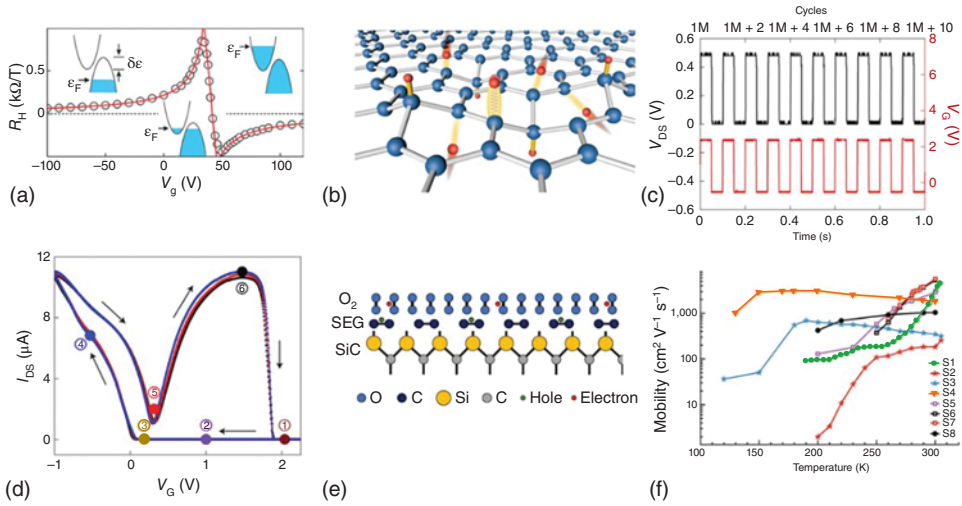


**Figure 1.17** (a) Hall coefficient  $R_H$  of FLG versus  $V_G$  at  $T = 5$  K. *Source*: Reprinted with permission from Ref. [2]. (b) Schematic of hydrogenation process between the graphene lattice and  $\text{H}^+$  ions. (c)  $V_{DS}$  (left) measurement after 1M switching cycles with periodically changed  $V_G$  (right) between  $-0.5\text{V}$  and  $2.4\text{V}$ . (d) Three consecutive cycles of  $I_{DS}$  measurements in MLG versus  $V_G$  with fixed  $V_{DS} = 5\text{mV}$ . *Source*: Reprinted with permission from Ref. [93]. Copyright 2021, Springer Nature Limited. (e) Schematic of SEG p-doping process by charge transfer. (f) Hall mobilities of different SEG devices of S1–S8 versus temperature. *Source*: Reprinted with permission from Ref. [39]. Copyright 2024, Springer Nature Limited.

properties due to dehydrogenation. This reversible, hydrogen-induced conductor–insulator transition was completely observed in MLG (Figure 1.17d), BLG, and TLG with stable  $I_{DS}$ - $V_G$  curves. The hydrogenation strategy of graphene showed reliable gate-controlled switching capability, remaining operative without any degradation of  $V_{DS}$  after 1 million (1M) switching cycles of MLG-FETs (Figure 1.17c). Zhao et al. p-doped the SEG devices by charge transfer of adsorbed oxygen to exhibit the intrinsic transport properties of SEG on SiC (Figure 1.17e; see Section 1.2.1.2 for SEG growth method) [39]. With the gradual temperature increase in the 100–300 K range, the conductivity and Hall mobility of the samples also showed an increasing trend with maximum mobility of  $5500 \text{ cm}^2/(\text{V}\cdot\text{s})$  (Figure 1.17f). The mobilities of S2, S3, and S4 increased rapidly and then tended to saturate with the temperature increase, which reflected the transition of the transport mechanism from localized defect states in the bandgap to high-mobility band transport, confirming the semiconductor nature of SEG. The  $I_{ON}/I_{OFF}$  ratio of  $\sim 10^6$  and SS of  $\sim 60 \text{ mV/dec}$  obtained by the density of states calculations demonstrated that the properties of SEG were sufficient for digital electronic applications.

### 1.3.1.2 Optoelectronic Properties and Applications

The unique properties of graphene have likewise attracted extensive interest in optoelectronics, prompting the construction of a range of graphene-based optoelectronic devices such as photodetectors (PDs), modulators, and hybrids. However, a number of factors, such as low light absorption ( $\sim 2.3\%$ ), large dark currents arising from zero band-gap, and difficulty of separation and collection of ultrafast photocarriers, have limited

further development of graphene in optoelectronics [94]. Koepfli et al. adopted a metamaterial integration strategy to maximize light absorption and photogenerated carrier extraction and realized high bandwidth ( $>500$  GHz) and wide operating window (from  $<1400$  nm to  $>4200$  nm) for metamaterial graphene PD [95]. The metamaterial absorber consisted of a relatively simple stack of metal-insulator-MLG-metal-insulator layers to achieve an almost perfect light absorption (Figure 1.18a–e) [96–98]. The dipole resonators were connected with interdigitated metal contacts, and a thin silver layer was added underneath the thicker gold contact layer on every other line, which is the key to more efficient carrier extraction (Figure 1.18f). Under 1550-nm illumination, despite the low responsivity of PD ( $R_{\text{ext}} = 0.75$  mA/W and  $R_{\text{int}} = 1.57$  mA/W), the linear behavior of response allowed the PD to maximize the input power up to 100 mW (Figure 1.18), giving rise to high photocurrent and the highest graphene data rate of 132 Gbit/s so far. The

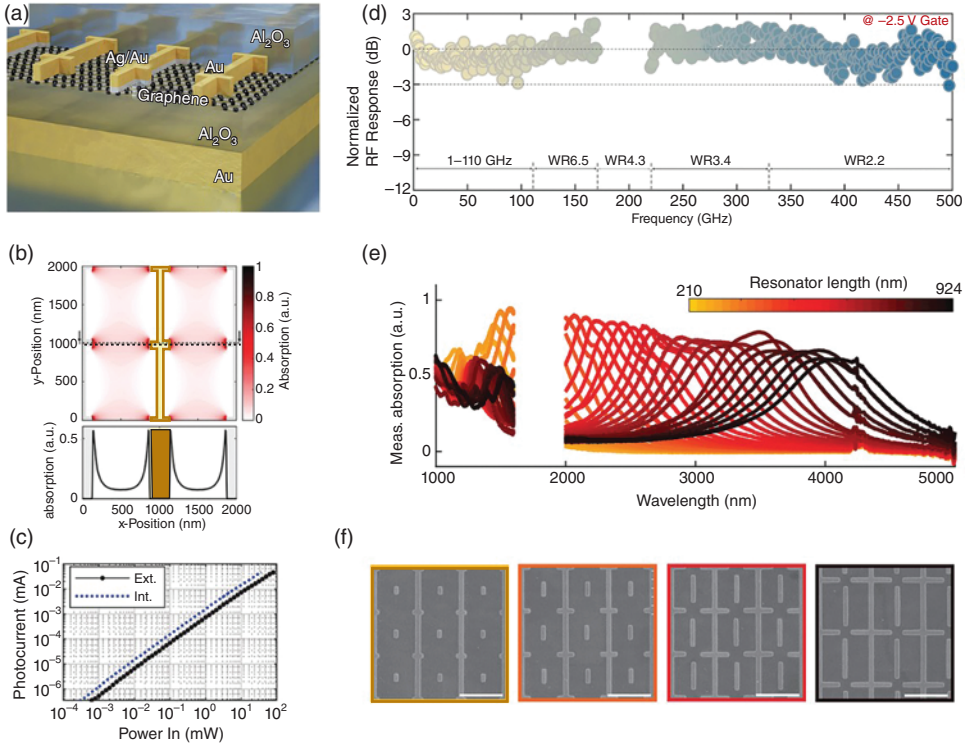


**Figure 1.18** (a) Schematic of Au-Al<sub>2</sub>O<sub>3</sub>-MLG-Ag/Au-Al<sub>2</sub>O<sub>3</sub> stacked metamaterial layers. (b) Absorption distribution with strong confinement close to the dipole resonators. (c) Extracted photocurrent for an optical input power sweep over five orders of magnitude (from  $10^{-3}$  to  $10^2$  mW). (d) Normalized frequency response of the graphene PD over a 2- to 500-GHz range. (e) Measured spectral absorption of different metamaterial dipole lengths, which shows the wavelength tunability. (f) Four example SEM images of polarization-independent design, where the colors correspond to the resonator-length scale bar shown in (e). Scale bar: 1  $\mu$ m. Source: Reprinted with permission from Ref. [95]. Copyright 2023, The American Association for the Advancement of Science.

high bandwidth of  $>500$  GHz was mainly attributed to shorter carrier transit time ( $\tau_{tr}$ ) (Figure 1.18), which was related to the structure design of the metamaterial. Through the direct alteration of dipole resonator length, the absorption spectra of PD revealed a tunable range of  $>3000$  nm (Figure 1.18), having potential in both sensing and telecommunication applications.

Stacking of monolayers enriches the optoelectronic applications of graphene. Construction of a homogeneous p-n junction is a common strategy to enhance the performance of graphene PDs since the bandgap of BLG could yield some optoelectronic properties beyond MLG [99]. Titova et al. demonstrated the enhancement of the sub-terahertz ( $f = 130$  GHz) response of split-gate BLG p-n junction PDs by an electrically induced bandgap (Figure 1.19a,b) [100, 101]. Bandgap induction at cryogenic temperature ( $\sim 25$  K) could improve the responsivity by enhancing the photo thermoelectric effect and emergence of tunneling rectification [102]. A larger bandgap was conducive to a higher thermoelectric optovoltage by increasing Seebeck coefficient  $S$  (Figure 1.19c), decreasing electronic heat conductance  $\chi_e$ , and decreasing hot carrier energy relaxation rate  $\tau e^{-1}$ . Bandgap induction also significantly optimized the noise equivalent power

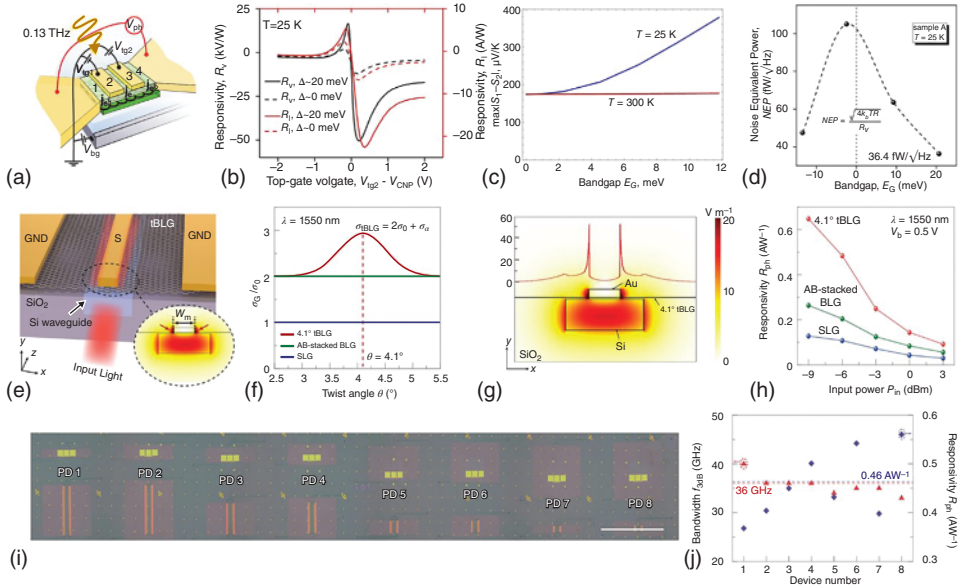


**Figure 1.19** (a) Schematic of split-gate BLG THz PD. (b) Comparison of current and voltage responsivity in the gapless (dashed lines) and gapped (solid lines) states. (c) Max  $|S_2 - S_1|$  as a function of  $E_G$  at charge neutral point. (d) Minimum attainable NEP for sample A versus  $E_G$  at  $T = 25$  K. *Source:* Reprinted with permission from [101]. Copyright 2023, American Chemical Society. (e) Schematic of Si waveguide-integrated tBLG PD. (f) Optical photoconductivity  $\sigma_g$  of tBLG versus twist angle  $\theta$ .  $\Delta E_{VHS}$  causes the transition  $\sigma_g$ . (g) Strong field localization around the metal/tBLG interface. (h) Power dependence of responsivity for tBLG, BLG, and SLG PDs at  $V_b = 0.5$  V. (i) Optical image of tBLG PDs array. Scale bar: 1 mm. (j) Statistical plot of responsivity and bandwidth from eight devices in (i), with average bandwidth and responsivity of 36 GHz and 0.46 A/W, respectively. *Source:* Reprinted with permission from Ref. [106]. Copyright 2024, Springer Nature Limited.

(NEP) of BLG p-n junctions from  $100 \text{ fW/Hz}^{1/2}$  at zero bandgap down to  $36 \text{ fW/Hz}^{1/2}$  at the maximum bandgap ( $\sim 25 \text{ meV}$ ) (Figure 1.19d). The NEP achieved a comparable level to commercially available detectors at a much lower degree of bandgap [103]. Furthermore, when two graphene layers are stacked with a twist angle  $\theta$ , the overlap and reconstruction of the Dirac cones produce van Hove singularities (vHS), which is quite different from the case of AB-stacked BLG [104]. The introduction of the vHS significantly enhances the light-matter interactions in twisted bilayer graphene (tBLG), and the energy gap between vHS ( $\Delta E_{\text{vHS}}$ ) can be tuned with the change of  $\theta$  [105]. Wu et al. demonstrated the potential of tBLG for applications of optical communications utilizing heterogeneous integration with silicon photonics (Figure 1.19e) [106]. Large-area controllable tBLG growth yielded a twist angle of  $\sim 4.1^\circ$  demonstrated by  $\Delta E_{\text{vHS}}$ -induced photoconductivity transition (Figure 1.19f). The incident electric field distribution simulation showed a strong localization at the electrode/tBLG interface, which is favorable for tBLG absorption (Figure 1.19g). Under  $1550 \text{ nm}$  incident wavelength, tBLG-integrated PD exhibited a high responsivity of  $0.65 \text{ A/W}$ , which was superior to that of AB-stacked BLG and MLG (Figure 1.19h), and showed uniform performance across eight individual devices and an 8-device array on silicon waveguide (Figure 1.19i,j). The bandwidth analysis showed a bandwidth of over  $65 \text{ GHz}$  and a high data rate of  $50 \text{ Gbit/s}$ , indicating the high sensitivity of tBLG PD.

#### 1.3.1.3 Spintronic Properties

Unlike the parabolic  $E$ - $k$  relationship in conventional semiconductors such as Si, the linear  $E$ - $k$  relationship in graphene enables its carriers to exhibit Dirac fermion-like behavior with near-zero mass and high Fermi velocity ( $v_F \sim 10^6 \text{ m/s}$ ) [86, 107]. Spin-orbit coupling (SOC) in graphene triggers many novel physical effects, such as the quantum Hall effect, spin Hall effect, spin quantum Hall effect, and quantum anomalous Hall effect (QAHE) [108]. Recently, Sha et al. observed the ferromagnetic state in rhombohedral (ABCA)-stacked tetralayer graphene (4LG) through graphene/ $\text{WSe}_2$  heterostructure (Figure 1.20a) [109]. The proximity-induced SOC by  $\text{WSe}_2$  and spontaneous time-reversal symmetry breaking in ABCA-stacked 4LG led to the observation of QAHE in graphene. At a vertical displacement field of  $D = -0.1 \text{ V/nm}$ , transport measurements on ABCA-4LG/ $\text{WSe}_2$  showed ferromagnetism and Hall resistance quantization (Figure 1.20b,c), which was further demonstrated as a Chern insulator with Chern number of four. Besides, ABCA-4LG with  $\text{WSe}_2$  exhibited a sequential transition of layer-antiferromagnetic (LAF) insulator, Chern insulator (CI), and layer-polarized insulator (LPI) states when  $|D|$  was increased from zero. In contrast, the intermediate CI state was not observed in 4LG without  $\text{WSe}_2$ , suggesting that the  $\text{WSe}_2$ -induced SOC had a crucial role in the ferromagnetism generation of 4LG (Figure 1.20d,e). More interestingly, the ferromagnetism in ABCA-4LG/ $\text{WSe}_2$  heterostructure could be modulated not only by magnetic field but also by displacement field and carrier concentration.

#### 1.3.1.4 Superconductive Properties

The unconventional superconductivity of graphene was experimentally observed by Cao et al. in a tBG system near a slight “magic angle” ( $\theta \sim 1.1^\circ$ ) (Figure 1.21a) [110, 111]. Previously, Bistritzer et al. had predicted the electronic structure of tBG varying

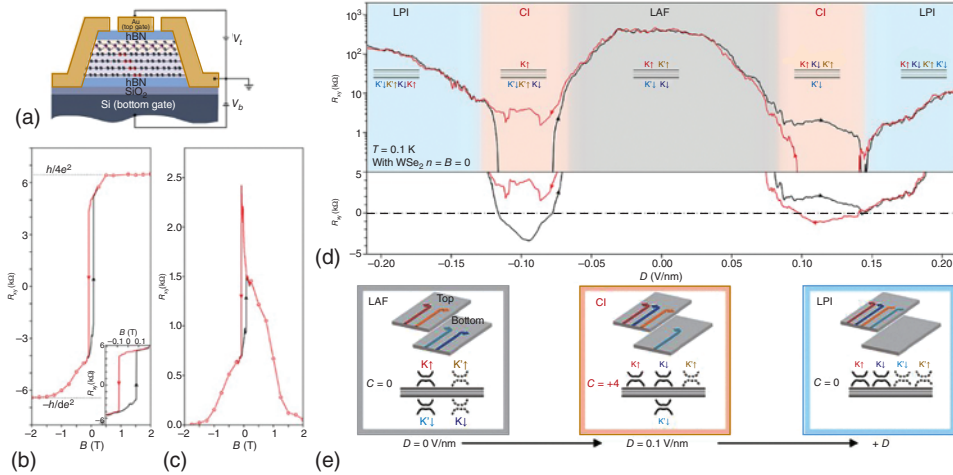


**Figure 1.20** (a) Schematic of a dual-gate WSe<sub>2</sub>/ABCA-4LG device. (b, c) Magnitude field-dependent (b) Hall resistance  $R_{xy}$  and (c) longitudinal resistance  $R_{xx}$  at  $D = -0.1$  V/nm,  $T = 0.1$  K. (d)  $R_{xy}$  as a function of  $D$  at  $B = 0$  in ABCA-4LG with SOC (WSe<sub>2</sub>). Insets (d) indicate the layer polarization of spin-valley flavors for different broken-symmetry states. (e) Schematics of the Chern numbers and Hall conductivity contributions of four spin-valley flavor pairs for different broken-symmetry states. *Source:* Reprinted with permission from Ref. [109]. Copyright 2024, The American Association for the Advancement of Science.

with periodic Moiré pattern, in which strong interlayer coupling leads to a flat energy band structure as  $\theta$  approaches the “magic angle” [112]. The  $v_F$  of electrons in these flat bands is significantly reduced and macroscopically manifests as a Mott-like insulating state of tBG, as confirmed in the experiments of Cao et al. (Figure 1.21c) [111]. Moreover, measurements of the conductance of magic-angle tBG (MATBG) at 70 mK showed a typical V-shaped conductance caused by the renormalized Dirac cones near the charge neutrality point ( $n = 0$ ). However, they indicated the suppression of a superconducting state by a magnetic field in the vicinity of  $-2$  electrons per Moiré unit cell (Figure 1.21b). In Figure 1.21c, a superconducting region was also observed near the Mott state with the highest critical temperature  $T_c \sim 1.7$  K. More peculiarly, the carrier concentration leading to this  $T_c$  was merely  $1.5 \times 10^{11} \text{ cm}^{-2}$ , which could be only explained by strong electron–electron interactions. Besides tBLG, the superconductivity can be realized in other stacked systems of graphene as well, such as ABC-TLG/h-BN heterostructure [113].

Researchers have been actively exploring applications of superconductivity in MATBG. An example given by Klein et al. is the reproducible bistability switching of MATBG between superconductor, metal, and correlated insulator states (Figure 1.21d,e) [114]. This bistability was accomplished through the gate hysteresis in the top-BN/MATBG/bottom-BN dual-gate structure [115], which could be readily controlled by gate voltage regulation (Figure 1.21 f,g). Characterization of the superconducting state with filling factor



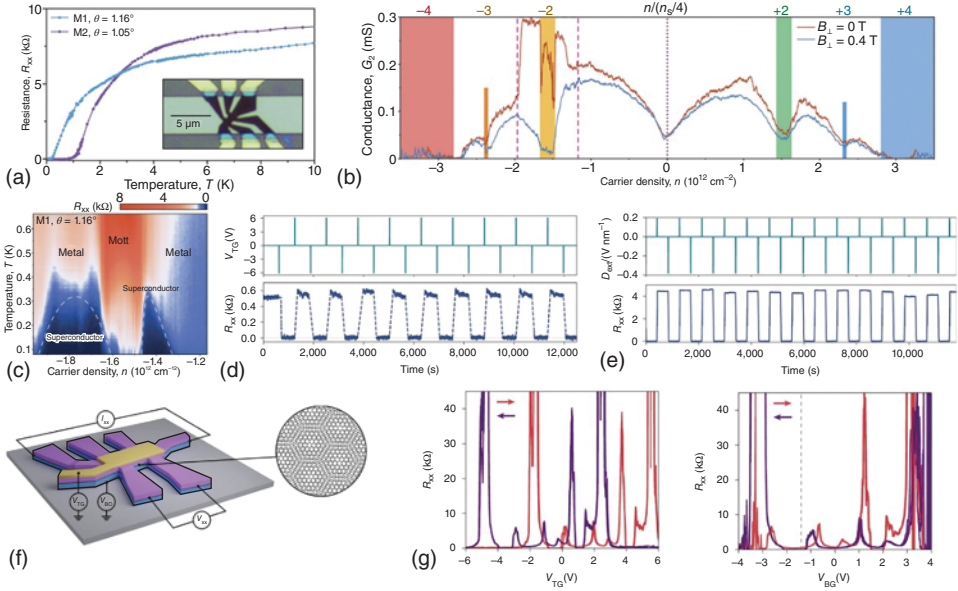


**Figure 1.21** (a) Four-probe resistance  $R_{xx}$  of two devices, M1 and M2, with  $\theta = 1.16^\circ$  and  $\theta = 1.05^\circ$ , respectively. Inset: optical image of M1. (b) Two-probe conductance  $G_2$  of M1 measured in  $B_\perp = 0$  T (red) and  $B_\perp = 0.4$  T (blue). (c) Measured  $R_{xx}$  of M1 versus carrier density ( $n$ ) and temperature ( $T$ ). Metal, Mott, and superconductor regions are labeled. *Source:* Reprinted with permission from Ref. [111]. Copyright 2018, Springer Nature Limited. (d) Switching between metal and superconducting states with top-gate voltage  $V_{TG} = \pm 6$  V and fixed bottom-gate voltage  $V_{BG} = -1.4$  V under  $T = 65$  mK. (e) Switching between correlated insulator and superconducting states with alternating displacement field  $D_{ext}$  and fixed carrier density  $n_{ext}$  under  $T = 65$  mK. (f) Schematic of dual-gate MATBG device in a Hall bar geometry. Inset: moiré pattern of the MATBG heterostructure. (g)  $R_{xx}$  versus  $V_{TG}$  and  $V_{BG}$  with sweep directions up and down. *Source:* Reprinted with permission from Ref. [114]. Copyright 2023, Springer Nature Limited.

$\nu = \pm(2 + \delta)$  demonstrated its robustness on both electron and hole sides, leading to highly tunable MATBG superconducting devices.

### 1.3.2 Carbon Nanotubes

Since CNTs can be considered as rolled-up graphene layers, the carrier transport properties of CNTs are similar to those of graphene. However, unlike the zero-bandgap characteristics of graphene, the metallic or semiconductive properties of CNTs are determined by whether or not the chiral vector ( $n, m$ ) crosses the Dirac K-points [49], which is equivalent to judge whether  $\text{mod}(2n + m, 3)$  is equal to zero. Metallic CNTs are satisfied with the relation  $\text{mod}(2n + m, 3) = 0$ , while semiconductive CNTs are not (Figure 1.8b). Therefore, CNTs exhibiting metallic and semiconductive properties should account for 1/3 and 2/3 of the total [49, 116].

Semiconductive SWCNTs can also be grouped into Type I or II with  $\text{mod}(2n + m, 3) = 1$  or 2, and those with the same  $2n + m$  value are classified as the same family [117].

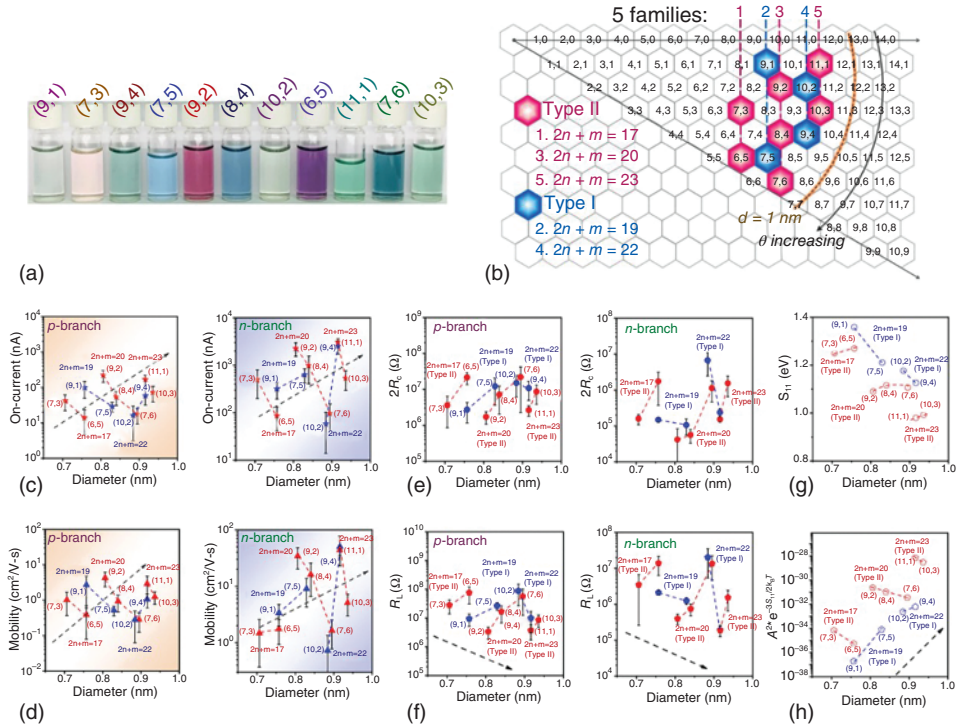


**Figure 1.22** (a) Photograph of single-chirality SWCNT solutions. (b) SWCNTs with different types and families are on the chiral map. (c) On-current, (d) mobility, (e)  $2R_C$ , and (f)  $R_L$  of both p- and n-branch of SWCNTs as a function of diameter from statistical data. (g)  $S_{11}$  and (h)  $A^2 e^{-3S_{11}/2k_B T}$  of SWCNTs as a function of diameter from further analysis. *Source:* Reprinted with permission from Ref. [118]. Copyright 2023, Springer Nature Limited.

Su et al. prepared 11 different types of single-chirality SWCNTs for electrical measurements by effective separation and purification (Figure 1.22a,b) [118, 119]. Electrical measurements, along with resistance analysis of SWCNTs, were carried out based on density-controlled SWCNT thin film transistors. Different types of semiconductive SWCNTs showed opposite trends of transport properties as the chiral angle increased. Specifically, for Type II SWCNTs, the on-current and mobility of both p- and n-branch within the same family decreased with increasing chiral angle, while it was contrary for Type I (Figure 1.22c,d). Measurements of various resistance components in SWCNT films, such as contact resistance ( $R_C$ ) and channel resistance ( $R_L$ ), also showed a similar dependence on the chiral angle (Figure 1.22e,f). By further analysis,  $R_C$  and  $R_L$  can be respectively attributed to the first bandgap ( $S_{11}$ ) and relative junction conductance  $G_{ij}^{NT} = A^2 \exp [(-3S_{11})/2k_B T]$  of SWCNTs, showing a chiral dependence consistent with  $R_C$  and  $R_L$  (Figure 1.22g,h). However, experimental results in the p-branch of  $2n + m = 19$  family were not by theoretical predictions, possibly due to interference from impurities or interfacial states. The systematic study on the relationship between

chirality and electrical properties of semiconductive SWCNTs is instructive for the design of SWCNT devices.

The 1D morphology of CNTs facilitates the assembly of high-density, highly aligned arrays, which is a significant advantage for high-performance CNT-FETs, especially in the post-Moore era with shrinking feature sizes. Lin et al. reported aligned CNT-FETs with promising applications when scaled down to a sub-10 nm node [120]. With a contact gate pitch (CGP) of 175 nm (Figure 1.23a), CNT-FETs showed excellent p-type performance with an on current ( $I_{ON}$ ) of 2.24 mA/ $\mu\text{m}$  and a peak transconductance ( $g_m$ ) of 1.64 mS/ $\mu\text{m}$ , which is superior to the 45 nm silicon technology node (CGP = 160 nm). A CNT-FET-based six-transistor (6T) static random access memory (SRAM) was also fabricated at 175 nm CGP with an area of 0.976  $\mu\text{m}^2$  (Figure 1.23b), which improved the integration density while avoiding complex silicon-based back-end interconnections. To further scale down to a 10 nm node (CGP  $\sim$  54 nm), a full-contact structure was employed for CNT-FETs, which significantly reduced the contact resistance while combining the benefits of side-contact and end-contact structures (Figure 1.23c,d). By scaling the gate length ( $L_g$ ) and contact length ( $L_{con}$ ) down to 35 nm and 20 nm (CGP  $\sim$  61 nm), an  $I_{ON}$  of 2.43 mA/ $\mu\text{m}$  and a  $g_m$  of 2.45 mS/ $\mu\text{m}$  were achieved, which are comparable to the performance of Si- P-Channel Metal Oxide Semiconductor Field Effect Transistors (PMOSFETs) at 10 nm node (Figure 1.23e) [121].

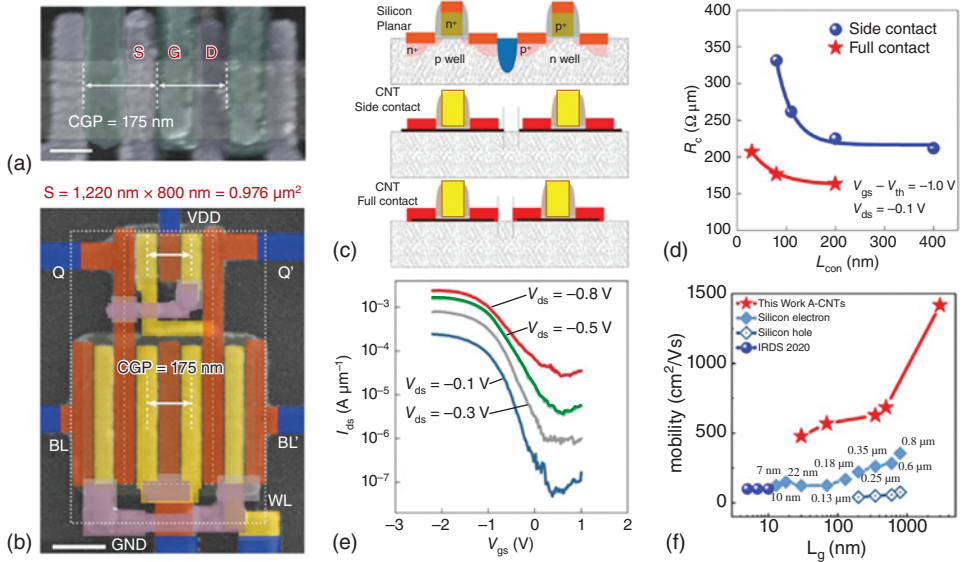


**Figure 1.23** (a) False-color SEM image of three top-gated CNT-FETs in series with shared source/drain contacts with 175 nm CGP. Scale bar: 100 nm. (b) False-color SEM image of CNT 6T SRAM cell with 175 nm CGP. Scale bar: 200 nm. (c) Schematic of the silicon planar structure, CNT side-contact structure, and CNT full-contact structure. (d)  $R_c$  versus  $L_{con}$  for side-contact and full-contact structure. (e) Transfer characteristics of the ultrascaled CNT-FET with 61 nm CGP. (f) Benchmarking the mobility of CNT-FETs at different  $L_g$  with that of Si FETs from Intel and IRDS 2020. Source: Reprinted with permission from Ref. [120]. Copyright 2023, Springer Nature Limited.

More attractively, the mobility of CNT-FETs is at least four times higher than the electron or hole mobility of Si transistors at any gate length (Figure 1.23f), highlighting the great value for applications in digital integrated circuits.

Unlike 2D graphene, 1D CNT has a direct bandgap that is inversely proportional to its diameter ( $E_g \sim 0.7 \text{ eV}/d \text{ (nm)}$ ) [122, 123], which enables arrays or thin films of CNTs with different diameters to cover a wide spectrum for photodetection [124]. Also, photo-excited electron-hole pairs interact strongly in the confined space of 1D CNTs, leading to large exciton binding energies. Hence, exciton behavior significantly impacts the performance of CNT optoelectronic devices [125]. Wu et al. demonstrated a high-density array CNT PD operational in 2- $\mu\text{m}$  band photodetection, which provides a viable solution for high-speed optical communications (Figure 1.24a,b) [122]. The CNT arrays showed high alignment with the degree of polarization  $P \sim 89\%$ , and the estimated  $E_g \sim 0.48 \text{ eV}$  of CNTs demonstrated the ability for 2- $\mu\text{m}$  band communications. To reduce the bandwidth limitation by resistance–conductance time constant, quartz was selected as the substrate of CNT PD, which effectively reduced parasitic capacitance and achieved a low total capacitance of  $\sim 12 \text{ fF}$  (Figure 1.24c). At an incident wavelength of

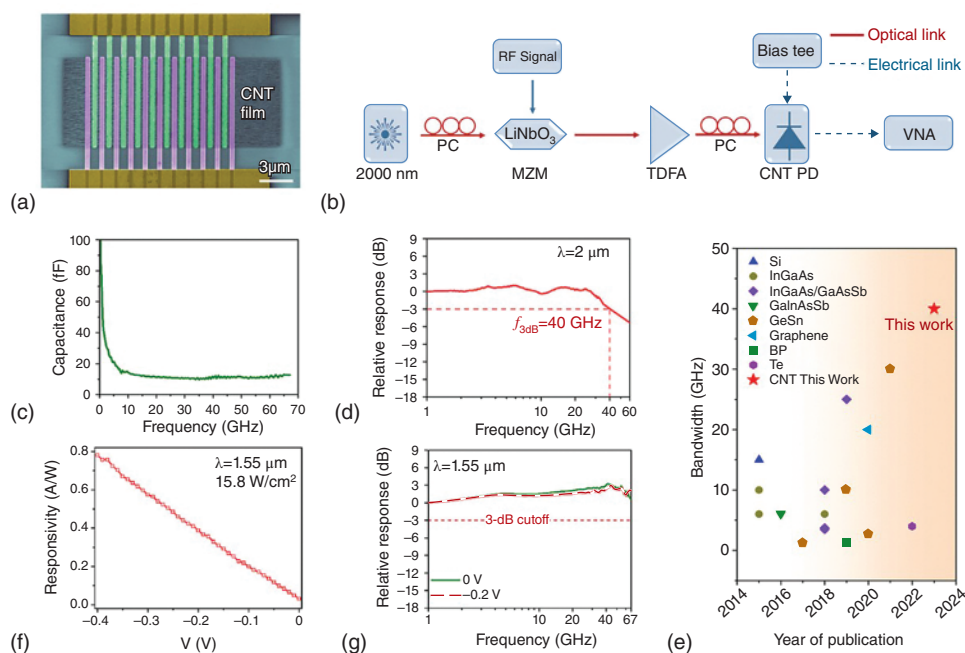


**Figure 1.24** (a) False-colored SEM image of aligned CNT PD with a channel length of 200 nm and a total channel width of 200  $\mu\text{m}$ . (b) Frequency response measurement setup of CNT PD at 2  $\mu\text{m}$ . (c) The capacitance of CNT PD as a function of frequency. (d) At  $V = -0.2 \text{ V}$ , the relative response of CNT PD versus modulation frequency with  $\lambda = 2 \mu\text{m}$ . (e) Benchmarking of bandwidth of state-of-the-art high-speed PDs at the 2  $\mu\text{m}$  band based on different materials. (f) The current responsivity of CNT PD versus  $V$  with  $\lambda = 1.55 \mu\text{m}$ . (g) At different  $V = 0$  and  $V = -0.2 \text{ V}$ , the relative response of CNT PD versus modulation frequency with  $\lambda = 1.55 \mu\text{m}$ . Source: Reprinted with permission from Ref. [122]. Copyright 2023, American Chemical Society.

2  $\mu\text{m}$ , CNT PD achieved a current responsivity of up to 0.62 A/W (Figure 1.24d), an NEP of  $<10 \text{ pW/Hz}^{1/2}$ , and a bandwidth of  $>40 \text{ GHz}$ , which is higher than any other state-of-the-art high-speed PDs in recent years (Figure 1.24e,f). In the commonly used band of 1.55  $\mu\text{m}$ , CNT PD also achieved an outstanding performance of  $>67 \text{ GHz}$  bandwidth and 0.78 A/W responsivity (Figure 1.24g), revealing the great potential of CNT-based optoelectronic devices for high-speed, low-power optical applications.

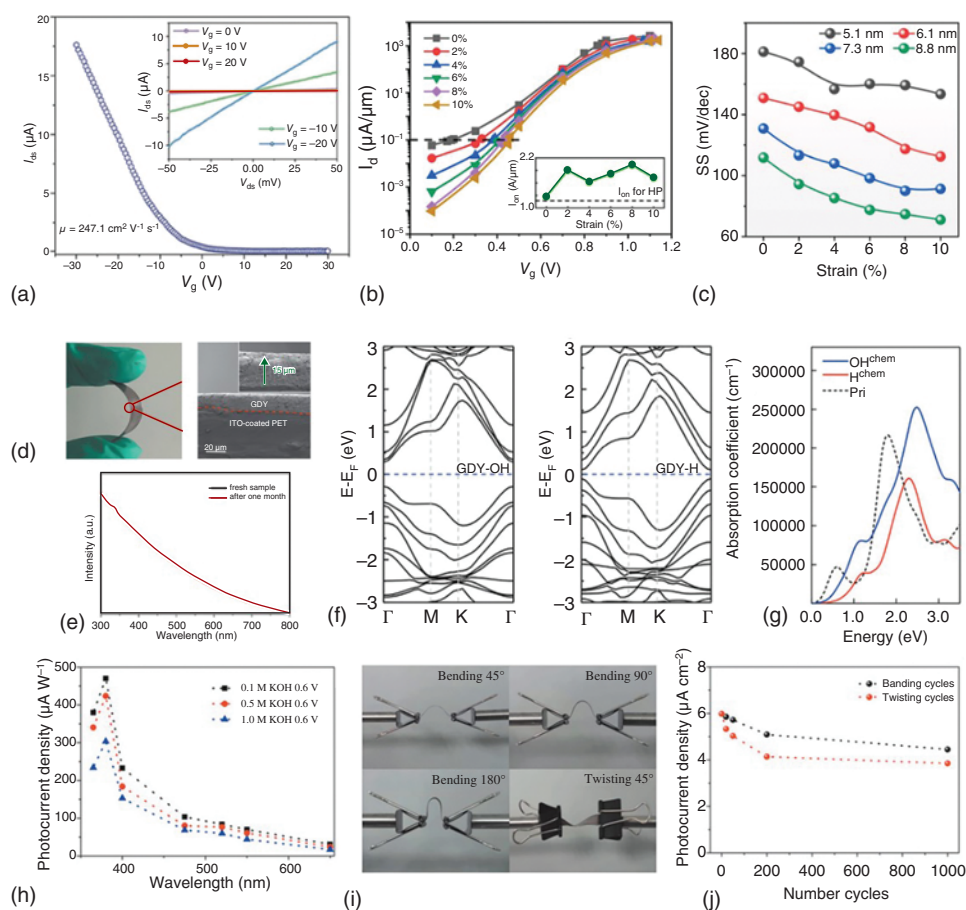


**Figure 1.25** (a) Transfer characteristics of ML-GDY FET at  $V_{ds} = 0.05 \text{ V}$ . Inset: Output characteristics under various  $V_g$  from  $-20 \text{ V}$  to  $20 \text{ V}$ . Source: Reprinted with permission from Ref. [78]. Copyright 2023, Wiley-VCH GmbH. (b) Strain-dependent transfer characteristics of GDY-FET with a channel length of 7.3 nm. Inset:  $I_{ON}$  under different strains. (c) SS of GDY-FET with different channel lengths versus strain. Source: Reprinted with permission from Ref. [127]. Copyright 2020, Elsevier B.V. (d) Digital macrograph and SEM image of the PD with GDY thickness of 15  $\mu\text{m}$ . (e) UV-vis absorption spectra of GDY PD. (f) Band structures of  $\text{OH}^-$  and  $\text{H}^+$  chemically adsorbed GDY. (g) Comparison of the absorption spectra between pristine GDY and GDY with  $\text{OH}^-$  and  $\text{H}^+$  adsorption. (h) Responsivity of GDY PD versus incident wavelength at different KOH concentrations. (i) Photographs of GDY PD bending and twisting tests. (j) Photocurrent density of GDY PD versus number cycles of bending (black) and twisting (red) tests. Source: Reprinted with permission from Ref. [128]. Copyright 2020, Wiley-VCH Verlag GmbH & Co. KGaA, Weinheim.



### 1.3.3 Graphyne

Unlike graphene, GDY has a bandgap of  $\sim 1.04$  eV, which is close to the bandgap value of silicon. However, the direct nature of bandgap may allow GDY to yield superior electronic and optoelectronic performance to silicon [78, 126]. Li et al. applied the prepared ML-GDY (see Section 1.2.3.1 for synthesis method) to FETs and measured an average mobility of  $231.4 \text{ cm}^2/(\text{V}\cdot\text{s})$  and a switching ratio of  $1.2 \times 10^3$  (Figure 1.25a), indicating potential FET applications [78]. Previously, most electrical characterizations were performed based on multilayer GDY due to the difficulty of preparing high-quality ML-GDY. The bandgap of GDY can be modified in several approaches, such as the strain-engineering strategy introduced in GDY-FETs by Sang et al. [127]. Biaxial tensile strain significantly increased the bandgap of GDY, which suppressed the leakage current in GDY-FETs and optimized the subthreshold swing (SS) (Figure 1.25b,c). Due to the sub-10 nm scaling of the channel, the increased bandgap significantly reduced the off-state tunneling current by increasing the potential barrier  $\phi_B$  between source and drain, which inhibited scaling-induced performance degradation and drastically improved the performance of GDY-FETs.

Moreover, various C–C bond composition and highly conjugated 2D planar system of GDY enable great structural flexibility [129]. Zhang et al. prepared a flexible PD by spin-coating GDY onto flexible polyethylene terephthalate substrates (Figure 1.25d) [128]. GDY PD possessed a long-term stable light absorption in the short-wavelength range of 300–800  $\mu\text{m}$  (Figure 1.25e), which is enhanced by the alkaline environment provided by the KOH electrolyte. GDY with a hollow triangle configuration can adsorb exotic  $\text{H}^+$  or  $\text{OH}^-$  ions, where smaller  $\text{H}^+$  is easily trapped by the porous structure, leading to more significant *ab* in-plane distortions of GDY. In contrast, low-concentration  $\text{OH}^-$  can be distributed on the GDY surface, inducing out-of-plane distortion without affecting the *ab* in-plane GDY framework, which leads to a larger bandgap and stronger absorption of GDY (Figure 1.25f,g). GDY PD measured in the KOH environment showed the highest responsivity of  $1086.96 \mu\text{A}\cdot\text{W}^{-1}$  at 380 nm wavelength and maintained a stable absorption performance after 1000 cycles of bending and twisting tests (Figure 1.25h–j).

## 1.4 Conclusion

This chapter briefly reviews the fabrication, properties, and applications of the representative carbon nanomaterials graphene, CNTs, and GY. Relevant research advances demonstrate the impressive properties and prospects of carbon nanomaterials. Represented by graphene, carbon nanomaterials are considered to be one of the candidates for replacing silicon and perpetuating Moore's law in transistor-based microelectronics. However, these materials do not yet have the mass production capability comparable to silicon-based technology. As graphene celebrates its 20<sup>th</sup> anniversary, while researchers continue to explore the novel phenomena induced by carbon-based nanomaterials, it is still necessary to keep looking for ways to build a bridge from proof-of-concept to large-scale applications.

## References

- 1 Ehrenfreund, P., Irvine, W., Becker, L., Blank, J., Brucato, J.R., Colangeli, L., Derenne, S., Despois, D., Dutrey, A., Fraaije, H., Lazcano, A., Owen, T., Robert, F., ISSI-Team, A.I.S.S.I. Astrophysical and astrochemical insights into the origin of life. *Rep. Prog. Phys.* 2002, 65 (10): 1427–1487.
- 2 Novoselov, K.S., Geim, A.K., Morozov, S.V., Jiang, D., Zhang, Y., Dubonos, S.V., Grigorieva, I.V., Firsov, A.A. Electric field effect in atomically thin carbon films. *Science* 2004, 306 (5696): 666–669.
- 3 Li, X., Wang, X., Zhang, L., Lee, S., Dai, H. Chemically derived, ultrasmooth graphene nanoribbon semiconductors. *Science* 2008, 319 (5867): 1229–1232.
- 4 Iijima, S. Helical microtubules of graphitic carbon. *Nature* 1991, 354 (6348): 56–58.
- 5 Li, G., Li, Y., Liu, H., Guo, Y., Li, Y., Zhu, D. Architecture of graphdiyne nanoscale films. *Chem. Commun.* 2010, 46 (19): 3256.
- 6 Kroto, H.W., Heath, J.R., O'Brien, S.C., Curl, R.F., Smalley, R.E. C<sub>60</sub>: Buckminsterfullerene. *Nature* 1985, 318 (6042): 162–163.
- 7 Xu, X., Ray, R., Gu, Y., Ploehn, H.J., Gearheart, L., Raker, K., Scrivens, W.A. Electrophoretic analysis and purification of fluorescent single-walled carbon nanotube fragments. *J. Am. Chem. Soc.* 2004, 126 (40): 12736–12737.
- 8 Geim, A.K., Novoselov, K.S. The rise of graphene. *Nat. Mater.* 2007, 6 (3): 183–191.
- 9 Landau, L.D. Zur Theorie Der Phasenumwandlungen II. *Phys. Z Sowjetunion* 1937, 11 (545): 26–35.
- 10 Peierls, R. Quelques Propriétés Typiques Des corps solides. In: *Annales de l'institut Henri Poincaré* 1935, 5: 177–222.
- 11 Land, T., Michely, T., Behm, R., Hemminger, J., Comsa, G. STM investigation of single layer graphite structures produced on Pt (111) by hydrocarbon decomposition. *Surf. Sci.* 1992, 264 (3): 261–270.
- 12 Dresselhaus, M.S., Dresselhaus, G. Intercalation compounds of graphite. *Adv. Phys.* 2002, 51 (1): 1–186.
- 13 Wang, X.-Y., Narita, A., Müllen, K. Precision synthesis versus bulk-scale fabrication of graphenes. *Nat. Rev. Chem.* 2017, 2 (1): 0100.
- 14 Moon, J.-Y., Kim, M., Kim, S.-I., Xu, S., Choi, J.-H., Whang, D., Watanabe, K., Taniguchi, T., Park, D.S., Seo, J., Cho, S.H., Son, S.-K., Lee, J.-H. Layer-engineered large-area exfoliation of graphene. *Sci. Adv.* 2020, 6 (44): eabc6601.
- 15 Shim, J., Bae, S.-H., Kong, W., Lee, D., Qiao, K., Nezich, D., Park, Y.J., Zhao, R., Sundaram, S., Li, X., Yeon, H., Choi, C., Kum, H., Yue, R., Zhou, G., Ou, Y., Lee, K., Moodera, J., Zhao, X., Ahn, J.-H., Hinkle, C., Ougazzaden, A., Kim, J. Controlled crack propagation for atomic precision handling of wafer-scale two-dimensional materials. *Science* 2018, 362 (6415): 665–670.
- 16 Ming-Yuan, H., Hutchinson, J.W. Crack deflection at an interface between dissimilar elastic materials. *Int. J. Solids Struct.* 1989, 25 (9): 1053–1067.
- 17 Huang, Y., Pan, Y.-H., Yang, R., Bao, L.-H., Meng, L., Luo, H.-L., Cai, Y.-Q., Liu, G.-D., Zhao, W.-J., Zhou, Z., Wu, L.-M., Zhu, Z.-L., Huang, M., Liu, L.-W., Liu, L., Cheng, P., Wu, K.-H., Tian, S.-B., Gu, C.-Z., Shi, Y.-G., Guo, Y.-F., Cheng, Z.G., Hu, J.-P., Zhao, L.,

- Yang, G.-H., Sutter, E., Sutter, P., Wang, Y.-L., Ji, W., Zhou, X.-J., Gao, H.-J. Universal mechanical exfoliation of large-area 2D crystals. *Nat. Commun.* 2020, 11 (1): 2453.
- 18 Hernandez, Y., Nicolosi, V., Lotya, M., Blighe, F.M., Sun, Z., De, S., McGovern, I.T., Holland, B., Byrne, M., Gun'Ko, Y.K., Boland, J.J., Niraj, P., Duesberg, G., Krishnamurthy, S., Goodhue, R., Hutchison, J., Scardaci, V., Ferrari, A.C., Coleman, J.N. High-yield production of graphene by liquid-phase exfoliation of graphite. *Nat. Nanotechnol.* 2008, 3 (9): 563–568.
  - 19 León, V., Rodríguez, A.M., Prieto, P., Prato, M., Vázquez, E. Exfoliation of graphite with triazine derivatives under ball-milling conditions: preparation of few-layer graphene via selective noncovalent interactions. *ACS Nano* 2014, 8 (1): 563–571.
  - 20 Paton, K.R., Varrla, E., Backes, C., Smith, R.J., Khan, U., O'Neill, A., Boland, C., Lotya, M., Istrate, O.M., King, P., Higgins, T., Barwich, S., May, P., Puczkarski, P., Ahmed, I., Moebius, M., Pettersson, H., Long, E., Coelho, J., O'Brien, S.E., McGuire, E.K., Sanchez, B.M., Duesberg, G.S., McEvoy, N., Pennycook, T.J., Downing, C., Crossley, A., Nicolosi, V., Coleman, J.N. Scalable production of large quantities of defect-free few-layer graphene by shear exfoliation in liquids. *Nat. Mater.* 2014, 13 (6): 624–630.
  - 21 Ciesielski, A., Samorì, P. Graphene via sonication assisted liquid-phase exfoliation. *Chem. Soc. Rev.* 2014, 43 (1): 381–398.
  - 22 Liu, W., Zheng, X., Xu, Q. Supercritical CO<sub>2</sub> directional-assisted synthesis of low-dimensional materials for functional applications. *Small* 2023, 19 (33): 2301097.
  - 23 Romang, A.H., Watkins, J.J. Supercritical fluids for the fabrication of semiconductor devices: emerging or missed opportunities? *Chem. Rev.* 2010, 110 (1): 459–478.
  - 24 Jones, C.A., Zweber, A., DeYoung, J.P., McClain, J.B., Carbonell, R., DeSimone, J.M. Applications of “dry” processing in the microelectronics industry using carbon dioxide. *Crit. Rev. Solid State Mater. Sci.* 2004, 29 (3–4): 97–109.
  - 25 Zhu, H.-Y., Wang, Q.-B., Yin, J.-Z. High-pressure induced exfoliation for regulating the morphology of graphene in supercritical CO<sub>2</sub> system. *Carbon* 2021, 178: 211–222.
  - 26 Zhao, M., Casiraghi, C., Parvez, K. Electrochemical exfoliation of 2D materials beyond graphene. *Chem. Soc. Rev.* 2024, 53 (6): 3036–3064.
  - 27 Lee, H., Jin, S., Chung, J., Kim, M., Lee, S.W. Electrochemical production of two-dimensional atomic layer materials and their application for energy storage devices. *Chem. Phys. Rev.* 2023, 4 (1): 011306.
  - 28 Mirkhani, S.A., Iqbal, A., Kwon, T., Chae, A., Kim, D., Kim, H., Kim, S.J., Kim, M.-K., Koo, C.M. Reduction of electrochemically exfoliated graphene films for high-performance electromagnetic interference shielding. *ACS Appl. Mater. Interfaces* 2021, 13 (13): 15827–15836.
  - 29 Wang, S., Xue, J., Xu, D., He, J., Dai, Y., Xia, T., Huang, Y., He, Q., Duan, X., Lin, Z. Electrochemical molecular intercalation and exfoliation of solution-processable two-dimensional crystals. *Nat. Protoc.* 2023, 18 (9): 2814–2837.
  - 30 Yang, S., Zhang, P., Nia, A.S., Feng, X. Emerging 2D materials produced via electrochemistry. *Adv. Mater.* 2020, 32 (10): 1907857.
  - 31 Lu, X., Cai, M., Wu, X., Zhang, Y., Li, S., Liao, S., Lu, X. Controllable synthesis of 2D materials by electrochemical exfoliation for energy storage and conversion application. *Small* 2023, 19 (9): 2206702.
  - 32 Brodie, B.C. Sur Le Poids Atomique Du Graphite. *Ann. Chim. Phys.* 1860, 59: 466–472.

- 33 Staudenmaier, L. Verfahren Zur Darstellung Der Graphitsäure. *Berichte Dtsch. Chem. Ges.* 1898, 31 (2): 1481–1487.
- 34 Hummers, W.S., Offeman, R.E. Preparation of graphitic oxide. *J. Am. Chem. Soc.* 1958, 80 (6): 1339–1339.
- 35 Zelenák, F., Kováčová, M., Moravec, Z., Černák, M., Krumpolec, R. Fast, scalable, and environmentally friendly method for production of stand-alone ultrathin reduced graphene oxide paper. *Carbon* 2023, 215: 118436.
- 36 Tao, R., Li, F., Lu, X., Liu, F., Xu, J., Kong, D., Zhang, C., Tan, X., Ma, S., Shi, W., Mo, R., Lu, Y. High-conductivity–dispersibility graphene made by catalytic exfoliation of graphite for lithium-ion battery. *Adv. Funct. Mater.* 2021, 31 (6): 2007630.
- 37 Van Bommel, A.J., Crombeen, J.E., Van Tooren, A. LEED and auger electron observations of the SiC (0001) surface. *Surf. Sci.* 1975, 48 (2): 463–472.
- 38 Forbeaux, I., Themlin, J.-M., Debever, J.-M. Heteroepitaxial graphite on 6 H – SiC (0001): interface formation through conduction-band electronic structure. *Phys. Rev. B* 1998, 58 (24): 16396–16406.
- 39 Zhao, J., Ji, P., Li, Y., Li, R., Zhang, K., Tian, H., Yu, K., Bian, B., Hao, L., Xiao, X., Griffin, W., Dudeck, N., Moro, R., Ma, L., De Heer, W.A. Ultrahigh-mobility semiconducting epitaxial graphene on silicon carbide. *Nature* 2024, 625 (7993): 60–65.
- 40 De Heer, W.A., Berger, C., Ruan, M., Sprinkle, M., Li, X., Hu, Y., Zhang, B., Hankinson, J., Conrad, E. Large area and structured epitaxial graphene produced by confinement controlled sublimation of silicon carbide. *Proc. Natl. Acad. Sci.* 2011, 108 (41): 16900–16905.
- 41 Bao, J., Yasui, O., Norimatsu, W., Matsuda, K., Kusunoki, M. Sequential control of step-bunching during graphene growth on SiC (0001). *Appl. Phys. Lett.* 2016, 109 (8): 081602.
- 42 Sun, Z., Yan, Z., Yao, J., Beitler, E., Zhu, Y., Tour, J.M. Growth of graphene from solid carbon sources. *Nature* 2010, 468 (7323): 549–552.
- 43 Qi, T., Shao, Q., Qi, H., Xiao, J., Zhang, Y., Wang, Y., Jin, X., Chen, Y., Li, D., Zang, X., Cao, N. CVD growth of graphene on copper-plated scrap steel without external carbon source. *Nano Res.* 2023, 16 (10): 12263–12269.
- 44 Yi, X., Song, Q., Chen, Q., Zhao, C., Watanabe, K., Taniguchi, T., Chen, Q., Yan, C., Wang, S. Quantum transport in CVD graphene synthesized with liquid carbon precursor. *Nanotechnology* 2022, 33 (35): 355601.
- 45 Yu, Q., Lian, J., Siriponglert, S., Li, H., Chen, Y.P., Pei, S.-S. Graphene segregated on Ni surfaces and transferred to insulators. *Appl. Phys. Lett.* 2008, 93 (11): 113103.
- 46 Kim, K.S., Zhao, Y., Jang, H., Lee, S.Y., Kim, J.M., Kim, K.S., Ahn, J.-H., Kim, P., Choi, J.-Y., Hong, B.H. Large-scale pattern growth of graphene films for stretchable transparent electrodes. *Nature* 2009, 457 (7230): 706–710.
- 47 Li, X., Cai, W., An, J., Kim, S., Nah, J., Yang, D., Piner, R., Velamakanni, A., Jung, I., Tutuc, E., Banerjee, S.K., Colombo, L., Ruoff, R.S. Large-area synthesis of high-quality and uniform graphene films on copper foils. *Science* 2009, 324 (5932): 1312–1314.
- 48 Zhang, J., Liu, X., Zhang, M., Zhang, R., Ta, H.Q., Sun, J., Wang, W., Zhu, W., Fang, T., Jia, K., Sun, X., Zhang, X., Zhu, Y., Shao, J., Liu, Y., Gao, X., Yang, Q., Sun, L., Li, Q., Liang, F., Chen, H., Zheng, L., Wang, F., Yin, W., Wei, X., Yin, J., Gemming, T., Rummeli, M.H., Liu, H., Peng, H., Lin, L., Liu, Z. Fast synthesis of large-area bilayer graphene film on Cu. *Nat. Commun.* 2023, 14 (1): 3199.

- 49 Saito, R., Fujita, M., Dresselhaus, G., Dresselhaus, M.S. Electronic structure of chiral graphene tubules. *Appl. Phys. Lett.* 1992, 60 (18): 2204–2206.
- 50 Muhulet, A., Miculescu, F., Voicu, S.I., Schütt, F., Thakur, V.K., Mishra, Y.K. Fundamentals and scopes of doped carbon nanotubes towards energy and biosensing applications. *Mater. Today Energy* 2018, 9: 154–186.
- 51 Venkataraman, A., Amadi, E.V., Chen, Y., Papadopoulos, C. Carbon nanotube assembly and integration for applications. *Nanoscale Res. Lett.* 2019, 14 (1): 220.
- 52 Dresselhaus, M.S., Dresselhaus, G., Saito, R. Physics of carbon nanotubes. *Carbon* 1995, 33 (7): 883–891.
- 53 Liu, Y., Ge, Z., Li, Z., Chen, Y. High-power instant-synthesis technology of carbon nanomaterials and nanocomposites. *Nano Energy* 2021, 80: 105500.
- 54 Zain Mehdi, S.M., Shin, T.H., Abbas, S.Z., Kwon, H., Seo, Y., Kim, D., Hong, S.J., Goak, J.C., Lee, N. Superior field emission characteristics of highly crystalline and thermally stable carbon nanotubes grown in N<sub>2</sub> and O<sub>2</sub> by arc discharge. *Ceram. Int.* 2023, 49 (3): 4668–4676.
- 55 Ribeiro, H., Schnitzler, M.C., Da Silva, W.M., Santos, A.P. Purification of carbon nanotubes produced by the electric arc-discharge method. *Surf. Interfaces* 2021, 26: 101389.
- 56 Guo, T., Nikolaev, P., Thess, A., Colbert, D.T., Smalley, R.E. Catalytic growth of single-walled nanotubes by laser vaporization. *Chem. Phys. Lett.* 1995, 243 (1–2): 49–54.
- 57 Chen, S., Chen, Y., Xu, H., Lyu, M., Zhang, X., Han, Z., Liu, H., Yao, Y., Xu, C., Sheng, J., Xu, Y., Gao, L., Gao, N., Zhang, Z., Peng, L., Li, Y. Single-walled carbon nanotubes synthesized by laser ablation from coal for field-effect transistors. *Mater. Horiz.* 2023, 10 (11): 5185–5191.
- 58 Qin, X., Li, Y., Chernov, A.I., He, M., Zhao, W., Gao, Y., Li, Y., Qiu, S., Li, Q. Towards the preparation of single-walled carbon nanotubes with average diameter of 1.2 nm. *Carbon* 2024, 224: 119059.
- 59 Li, Y., Kim, W., Zhang, Y., Rolandi, M., Wang, D., Dai, H. Growth of single-walled carbon nanotubes from discrete catalytic nanoparticles of various sizes. *J. Phys. Chem. B* 2001, 105 (46): 11424–11431.
- 60 Zheng, J., Yang, R., Xie, L., Qu, J., Liu, Y., Li, X. Plasma-assisted approaches in inorganic nanostructure fabrication. *Adv. Mater.* 2010, 22 (13): 1451–1473.
- 61 Huang, S., Woodson, M., Smalley, R., Liu, J. Growth mechanism of oriented long single walled carbon nanotubes using “fast-heating” chemical vapor deposition process. *Nano Lett.* 2004, 4 (6): 1025–1028.
- 62 Zhu, Z., Cui, C., Bai, Y., Gao, J., Jiang, Y., Li, B., Wang, Y., Zhang, Q., Qian, W., Wei, F. Advances in precise structure control and assembly toward the carbon nanotube industry. *Adv. Funct. Mater.* 2022, 32 (11): 2109401.
- 63 Liu, F., Yuan, M., He, Y., Zhai, G., Xiang, H., Wu, Q., Zhu, M. Insights into the nucleation and structure of lignin-based carbon nanotubes synthesized using iron via floating catalyst chemical vapor deposition. *ACS Appl. Nano Mater.* 2024, 7 (7): 7184–7194.
- 64 Xu, Y., Miao, X., Chen, H., Gu, X., Liu, Y., Ma, C., Zhang, X., Zou, J. Fe complex-based catalyst system for the chirality-selected continuous synthesis of single-walled carbon nanotubes. *ACS Appl. Nano Mater.* 2024, 7 (5): 5525–5533.



- 65 Hou, P., Zhang, F., Zhang, L., Liu, C., Cheng, H. Synthesis of carbon nanotubes by floating catalyst chemical vapor deposition and their applications. *Adv. Funct. Mater.* 2022, 32 (11): 2108541.
- 66 Jiang, Q., Wang, F., Li, R., Li, B., Wei, N., Gao, N., Xu, H., Zhao, S., Huang, Y., Wang, B., Zhang, W., Wu, X., Zhang, S., Zhao, Y., Shi, E., Zhang, R. Synthesis of ultralong carbon nanotubes with ultrahigh yields. *Nano Lett.* 2023, 23 (2): 523–532.
- 67 Zhang, R., Zhang, Y., Zhang, Q., Xie, H., Qian, W., Wei, F. Growth of half-meter long carbon nanotubes based on Schulz–Flory distribution. *ACS Nano* 2013, 7 (7): 6156–6161.
- 68 Baughman, R.H., Eckhardt, H., Kertesz, M. Structure-property predictions for new planar forms of carbon: layered phases containing  $sp^2$  and  $sp$  atoms. *J. Chem. Phys.* 1987, 87 (11): 6687–6699.
- 69 Zheng, X., Chen, S., Li, J., Wu, H., Zhang, C., Zhang, D., Chen, X., Gao, Y., He, F., Hui, L., Liu, H., Jiu, T., Wang, N., Li, G., Xu, J., Xue, Y., Huang, C., Chen, C., Guo, Y., Lu, T.-B., Wang, D., Mao, L., Zhang, J., Zhang, Y., Chi, L., Guo, W., Bu, X.-H., Zhang, H., Dai, L., Zhao, Y., Li, Y. Two-dimensional carbon graphdiyne: advances in fundamental and application research. *ACS Nano* 2023, 17 (15): 14309–14346.
- 70 Li, H., Lim, J.H., Lv, Y., Li, N., Kang, B., Lee, J.Y. Graphynes and graphdienes for energy storage and catalytic utilization: theoretical insights into recent advances. *Chem. Rev.* 2023, 123 (8): 4795–4854.
- 71 Hu, G., He, J., Chen, J., Li, Y. Synthesis of a wheel-shaped nanographdiyne. *J. Am. Chem. Soc.* 2023, 145 (9): 5400–5409.
- 72 Zhou, J., Gao, X., Liu, R., Xie, Z., Yang, J., Zhang, S., Zhang, G., Liu, H., Li, Y., Zhang, J., Liu, Z. Synthesis of graphdiyne nanowalls using acetylenic coupling reaction. *J. Am. Chem. Soc.* 2015, 137 (24): 7596–7599.
- 73 Li, C., Lu, X., Han, Y., Tang, S., Ding, Y., Liu, R., Bao, H., Li, Y., Luo, J., Lu, T. Direct imaging and determination of the crystal structure of six-layered graphdiyne. *Nano Res.* 2018, 11 (3): 1714–1721.
- 74 Matsuoka, R., Sakamoto, R., Hoshiko, K., Sasaki, S., Masunaga, H., Nagashio, K., Nishihara, H. Crystalline graphdiyne nanosheets produced at a gas/liquid or liquid/liquid interface. *J. Am. Chem. Soc.* 2017, 139 (8): 3145–3152.
- 75 Xu, L., Sun, J., Tang, T., Zhang, H., Sun, M., Zhang, J., Li, J., Huang, B., Wang, Z., Xie, Z., Wong, W. Metallated graphynes as a new class of photofunctional 2D organometallic nanosheets. *Angew. Chem. Int. Ed.* 2021, 60 (20): 11326–11334.
- 76 Huang, R., Kou, Z., Rodriguez, R.D., Wang, X., Hou, Y., Wang, T., Zhang, T. Two-dimensional silver-metalated graphdiyne nanosheets for photocatalytic degradation of antibiotics. *ACS Appl. Nano Mater.* 2023, 6 (9): 7395–7403.
- 77 He, S., Wu, B., Xia, Z., Guo, P., Li, Y., Song, S. One-pot synthesis of gamma-graphyne supported pd nanoparticles with high catalytic activity. *Nanoscale Adv.* 2023, 5 (9): 2487–2492.
- 78 Li, J., Cao, H., Wang, Q., Zhang, H., Liu, Q., Chen, C., Shi, Z., Li, G., Kong, Y., Cai, Y., Shen, J., Wu, Y., Lai, Z., Han, Y., Zhang, J. Space-confined synthesis of monolayer graphdiyne in MXene interlayer. *Adv. Mater.* 2024, 36 (7): 2308429.
- 79 Yan, H., Yu, P., Han, G., Zhang, Q., Gu, L., Yi, Y., Liu, H., Li, Y., Mao, L. High-yield and damage-free exfoliation of layered graphdiyne in aqueous phase. *Angew. Chem. Int. Ed.* 2019, 58 (3): 746–750.

- 80 Liu, R., Gao, X., Zhou, J., Xu, H., Li, Z., Zhang, S., Xie, Z., Zhang, J., Liu, Z. Chemical vapor deposition growth of linked carbon monolayers with acetylenic scaffoldings on silver foil. *Adv. Mater.* 2017, 29 (18): 1604665.
- 81 Li, Q., Li, Y., Chen, Y., Wu, L., Yang, C., Cui, X. Synthesis of  $\gamma$ -graphyne by mechanochemistry and its electronic structure. *Carbon* 2018, 136: 248–254.
- 82 Lee, J., Li, Y., Tang, J., Cui, X. Synthesis of hydrogen substituted graphyne through mechanochemistry and its electrocatalytic properties. *Acta Phys.-Chim. Sin.* 2018, 34 (9): 1080–1087.
- 83 Fitzer, E., Kochling, K.-H., Boehm, H.P., Marsh, H. Recommended terminology for the description of carbon as a solid (IUPAC Recommendations 1995). *Pure Appl. Chem.* 1995, 67 (3): 473–506.
- 84 Boehm, H. Graphene—How a laboratory curiosity suddenly became extremely interesting. *Angew. Chem. Int. Ed.* 2010, 49 (49): 9332–9335.
- 85 Partoens, B., Peeters, F.M. From graphene to graphite: electronic structure around the K point. *Phys. Rev. B* 2006, 74 (7): 075404.
- 86 Wallace, P.R. The band theory of graphite. *Phys. Rev.* 1947, 71 (9): 622–634.
- 87 Castro Neto, A.H., Guinea, F., Peres, N.M.R., Novoselov, K.S., Geim, A.K. The electronic properties of graphene. *Rev. Mod. Phys.* 2009, 81 (1): 109–162.
- 88 Morozov, S.V., Novoselov, K.S., Katsnelson, M.I., Schedin, F., Elias, D.C., Jaszczak, J.A., Geim, A.K. Giant intrinsic carrier mobilities in graphene and its bilayer. *Phys. Rev. Lett.* 2008, 100 (1): 016602.
- 89 Zheng, Y., Sen, D., Das, S., Das, S. Graphene strain-effect transistor with colossal ON/OFF current ratio enabled by reversible nanocrack formation in metal electrodes on piezoelectric substrates. *Nano Lett.* 2023, 23 (7): 2536–2543.
- 90 Bai, Z., Xiao, Y., Luo, Q., Li, M., Peng, G., Zhu, Z., Luo, F., Zhu, M., Qin, S., Novoselov, K. Highly tunable carrier tunneling in vertical graphene-WS<sub>2</sub>-graphene van Der Waals heterostructures. *ACS Nano* 2022, 16 (5): 7880–7889.
- 91 Novoselov, K.S., Mishchenko, A., Carvalho, A., Castro Neto, A.H. 2D Materials and van Der Waals heterostructures. *Science* 2016, 353 (6298): aac9439.
- 92 Braga, D., Gutiérrez Lezama, I., Berger, H., Morpurgo, A.F. Quantitative determination of the band gap of WS<sub>2</sub> with ambipolar ionic liquid-gated transistors. *Nano Lett.* 2012, 12 (10): 5218–5223.
- 93 Li, S., Li, J., Wang, Y., Yu, C., Li, Y., Duan, W., Wang, Y., Zhang, J. Large transport gap modulation in graphene via electric-field-controlled reversible hydrogenation. *Nat. Electron.* 2021, 4 (4): 254–260.
- 94 Chen, X., Shehzad, K., Gao, L., Long, M., Guo, H., Qin, S., Wang, X., Wang, F., Shi, Y., Hu, W., Xu, Y., Wang, X. Graphene hybrid structures for integrated and flexible optoelectronics. *Adv. Mater.* 2020, 32 (27): 1902039.
- 95 Koepfli, S.M., Baumann, M., Koyaz, Y., Gadola, R., Güngör, A., Keller, K., Horst, Y., Nashashibi, S., Schwanninger, R., Doderer, M., Passerini, E., Fedoryshyn, Y., Leuthold, J. Metamaterial graphene photodetector with bandwidth exceeding 500 Gigahertz. *Science* 2023, 380 (6650): 1169–1174.
- 96 Landy, N.I., Sajuyigbe, S., Mock, J.J., Smith, D.R., Padilla, W.J. Perfect metamaterial absorber. *Phys. Rev. Lett.* 2008, 100 (20): 207402.

- 97 Xia, F., Mueller, T., Lin, Y., Valdes-Garcia, A., Avouris, P. Ultrafast graphene photodetector. *Nat. Nanotechnol.* 2009, 4 (12): 839–843.
- 98 Sagade, A.A., Neumaier, D., Schall, D., Otto, M., Pesquera, A., Centeno, A., Elorza, A. Z., Kurz, H. Highly air stable passivation of graphene based field effect devices. *Nanoscale* 2015, 7 (8): 3558–3564.
- 99 Tian, P., Tang, L., Teng, K.S., Xiang, J., Lau, S.P. Recent advances in graphene homogeneous p–n junction for optoelectronics. *Adv. Mater. Technol.* 2019, 4 (7): 1900007.
- 100 Mylnikov, D.A., Titova, E.I., Kashchenko, M.A., Safonov, I.V., Zhukov, S.S., Semkin, V.A., Novoselov, K.S., Bandurin, D.A., Svintsov, D.A. Terahertz photoconductivity in bilayer graphene transistors: evidence for tunneling at gate-induced junctions. *Nano Lett.* 2023, 23 (1): 220–226.
- 101 Titova, E., Mylnikov, D., Kashchenko, M., Safonov, I., Zhukov, S., Dzhikirba, K., Novoselov, K.S., Bandurin, D.A., Alymov, G., Svintsov, D. Ultralow-noise terahertz detection by p–n junctions in gapped bilayer graphene. *ACS Nano* 2023, 17 (9): 8223–8232.
- 102 Gayduchenko, I., Xu, S.G., Alymov, G., Moskotin, M., Tretyakov, I., Taniguchi, T., Watanabe, K., Goltsman, G., Geim, A.K., Fedorov, G., Svintsov, D., Bandurin, D.A. Tunnel field-effect transistors for sensitive terahertz detection. *Nat. Commun.* 2021, 12 (1): 543.
- 103 Icking, E., Banszerus, L., Wörtche, F., Volmer, F., Schmidt, P., Steiner, C., Engels, S., Hesselmann, J., Goldsche, M., Watanabe, K., Taniguchi, T., Volk, C., Beschoten, B., Stampfer, C. Transport spectroscopy of ultraclean tunable band gaps in bilayer graphene. *Adv. Electron. Mater.* 2022, 8 (11): 2200510.
- 104 Brihuega, I., Mallet, P., González-Herrero, H., Trambly De Laissardiére, G., Ugeda, M.M., Magaud, L., Gómez-Rodríguez, J.M., Ynduráin, F., Veuillen, J.-Y. Unraveling the intrinsic and robust nature of van Hove singularities in twisted bilayer graphene by scanning tunneling microscopy and theoretical analysis. *Phys. Rev. Lett.* 2012, 109 (19): 196802.
- 105 Jain, S.K., Juričić, V., Barkema, G.T. Structure of twisted and buckled bilayer graphene. *2D Mater.* 2016, 4 (1): 015018.
- 106 Wu, Q., Qian, J., Wang, Y., Xing, L., Wei, Z., Gao, X., Li, Y., Liu, Z., Liu, H., Shu, H., Yin, J., Wang, X., Peng, H. Waveguide-integrated twisted bilayer graphene photodetectors. *Nat. Commun.* 2024, 15 (1): 3688.
- 107 Novoselov, K.S., Geim, A.K., Morozov, S.V., Jiang, D., Katsnelson, M.I., Grigorieva, I.V., Dubonos, S.V., Firsov, A.A. Two-dimensional gas of massless Dirac fermions in graphene. *Nature* 2005, 438 (7065): 197–200.
- 108 Zhang, G., Wu, H., Yang, L., Jin, W., Zhang, W., Chang, H. Graphene-based spintronics. *Appl. Phys. Rev.* 2024, 11 (2): 021308.
- 109 Sha, Y., Zheng, J., Liu, K., Du, H., Watanabe, K., Taniguchi, T., Jia, J., Shi, Z., Zhong, R., Chen, G. Observation of a Chern insulator in crystalline ABCA-tetralayer graphene with spin-orbit coupling. *Science* 2024, 384 (6694): 414–419.
- 110 Cao, Y., Fatemi, V., Demir, A., Fang, S., Tomarken, S.L., Luo, J.Y., Sanchez-Yamagishi, J.D., Watanabe, K., Taniguchi, T., Kaxiras, E., Ashoori, R.C., Jarillo-Herrero, P. Correlated insulator behaviour at half-filling in magic-angle graphene superlattices. *Nature* 2018, 556 (7699): 80–84.

- 111 Cao, Y., Fatemi, V., Fang, S., Watanabe, K., Taniguchi, T., Kaxiras, E., Jarillo-Herrero, P. Unconventional superconductivity in magic-angle graphene superlattices. *Nature* 2018, 556 (7699): 43–50.
- 112 Bistritzer, R., MacDonald, A.H. Moiré bands in twisted double-layer graphene. *Proc. Natl. Acad. Sci.* 2011, 108 (30): 12233–12237.
- 113 Chen, G., Sharpe, A.L., Gallagher, P., Rosen, I.T., Fox, E.J., Jiang, L., Lyu, B., Li, H., Watanabe, K., Taniguchi, T., Jung, J., Shi, Z., Goldhaber-Gordon, D., Zhang, Y., Wang, F. Signatures of tunable superconductivity in a trilayer graphene Moiré superlattice. *Nature* 2019, 572 (7768): 215–219.
- 114 Klein, D.R., Xia, L.-Q., MacNeill, D., Watanabe, K., Taniguchi, T., Jarillo-Herrero, P. Electrical switching of a bistable Moiré superconductor. *Nat. Nanotechnol.* 2023, 18 (4): 331–335.
- 115 Zheng, Z., Ma, Q., Bi, Z., De La Barrera, S., Liu, M.-H., Mao, N., Zhang, Y., Kiper, N., Watanabe, K., Taniguchi, T., Kong, J., Tisdale, W.A., Ashoori, R., Gedik, N., Fu, L., Xu, S.-Y., Jarillo-Herrero, P. Unconventional ferroelectricity in Moiré heterostructures. *Nature* 2020, 588 (7836): 71–76.
- 116 Tang, D.-M., Cretu, O., Ishihara, S., Zheng, Y., Otsuka, K., Xiang, R., Maruyama, S., Cheng, H.-M., Liu, C., Golberg, D. Chirality engineering for carbon nanotube electronics. *Nat. Rev. Electr. Eng.* 2024, 1 (3): 149–162.
- 117 Samsonidze, G.G., Saito, R., Kobayashi, N., Grüneis, A., Jiang, J., Jorio, A., Chou, S.G., Dresselhaus, G., Dresselhaus, M.S. Family behavior of the optical transition energies in single-wall carbon nanotubes of smaller diameters. *Appl. Phys. Lett.* 2004, 85 (23): 5703–5705.
- 118 Su, W., Li, X., Li, L., Yang, D., Wang, F., Wei, X., Zhou, W., Kataura, H., Xie, S., Liu, H. Chirality-dependent electrical transport properties of carbon nanotubes obtained by experimental measurement. *Nat. Commun.* 2023, 14 (1): 1672.
- 119 Yang, D., Li, L., Li, X., Xi, W., Zhang, Y., Liu, Y., Wei, X., Zhou, W., Wei, F., Xie, S., Liu, H. Preparing high-concentration individualized carbon nanotubes for industrial separation of multiple single-chirality species. *Nat. Commun.* 2023, 14 (1): 2491.
- 120 Lin, Y., Cao, Y., Ding, S., Zhang, P., Xu, L., Liu, C., Hu, Q., Jin, C., Peng, L.-M., Zhang, Z. Scaling aligned carbon nanotube transistors to a sub-10 nm node. *Nat. Electron.* 2023, 6 (7): 506–515.
- 121 Auth, C., Aliyarukunju, A., Asoro, M., Bergstrom, D., Bhagwat, V., Birdsall, J., Bisnik, N., Buehler, M., Chikarmane, V., Ding, G., Fu, Q., Gomez, H., Han, W., Hanken, D., Haran, M., Hattendorf, M., Heussner, R., Hiramatsu, H., Ho, B., Jaloviar, S., Jin, I., Joshi, S., Kirby, S., Kosaraju, S., Kothari, H., Leatherman, G., Lee, K., Leib, J., Madhavan, A., Maria, K., Meyer, H., Mule, T., Parker, C., Parthasarathy, S., Peltó, C., Pipes, L., Post, I., Prince, M., Rahman, A., Rajamani, S., Saha, A., Santos, J.D., Sharma, M., Sharma, V., Shin, J., Sinha, R., Smith, R., Sprinkle, M., St Amour, A., Staus, C., Suri, R., Towner, D., Tripathi, A., Tura, A., Ward, C., Yeoh, A. A 10nm high performance and low-power CMOS technology featuring 3rd generation FinFET transistors, self-aligned quad patterning, contact over active gate and cobalt local interconnects. In: *2017 IEEE International Electron Devices Meeting (IEDM)*, IEEE, 2017.

- 122 Wu, W., Ma, H., Cai, X., Han, B., Li, Y., Xu, K., Lin, H., Zhang, F., Chen, Z., Zhang, Z., Peng, L.-M., Wang, S. High-speed carbon nanotube photodetectors for 2  $\mu\text{m}$  communications. *ACS Nano* 2023, 17 (15): 15155–15164.
- 123 Charlier, J.-C., Blase, X., Roche, S. Electronic and transport properties of nanotubes. *Rev. Mod. Phys.* 2007, 79 (2): 677–732.
- 124 Yang, L., Wang, S., Zeng, Q., Zhang, Z., Peng, L. Carbon nanotube photoelectronic and photovoltaic devices and their applications in infrared detection. *Small* 2013, 9 (8): 1225–1236.
- 125 Avouris, P., Freitag, M., Perebeinos, V. Carbon-nanotube photonics and optoelectronics. *Nat. Photonics* 2008, 2 (6): 341–350.
- 126 Fang, Y., Liu, Y., Qi, L., Xue, Y., Li, Y. 2D graphdiyne: an emerging carbon material. *Chem. Soc. Rev.* 2022, 51 (7): 2681–2709.
- 127 Sang, P., Ma, X., Wang, Q., Wei, W., Wang, F., Wu, J., Zhan, X., Li, Y., Chen, J. Toward high-performance monolayer graphdiyne transistor: strain engineering matters. *Appl. Surf. Sci.* 2021, 536: 147836.
- 128 Zhang, Y., Huang, P., Guo, J., Shi, R., Huang, W., Shi, Z., Wu, L., Zhang, F., Gao, L., Li, C., Zhang, X., Xu, J., Zhang, H. Graphdiyne-based flexible photodetectors with high responsivity and detectivity. *Adv. Mater.* 2020, 32 (23): 2001082.
- 129 He, J., Wang, N., Cui, Z., Du, H., Fu, L., Huang, C., Yang, Z., Shen, X., Yi, Y., Tu, Z., Li, Y. Hydrogen substituted graphdiyne as carbon-rich flexible electrode for lithium and sodium ion batteries. *Nat. Commun.* 2017, 8 (1): 1172.



